One-side heating test and modeling of tubular receivers equipped with turbulence promoters for solar tower applications

(Article begins on next page)

17 October 2022

One-side heating test and modeling of tubular receivers equipped with turbulence promoters for solar tower applications

Marco Cantone[1], Mattia Cagnoli[1], Jesus Fernandez Reche[2], Laura Savoldi[1*].

[1] Dipartimento Energia "Galileo Ferraris", Politecnico di Torino, Torino (Italy)

[2] CIEMAT, Plataforma Solar de Almería, Tabernas-Almería (Spain)

[*] *laura.savoldi@polito.it, corresponding author*

Abstract

Tubular receivers in central tower systems suffer the high mechanical stresses caused by the temperature gradient typically established along the tube and across its circumference due to the one side heating. In the present work, the thermal behavior of three different absorber tubes is investigated both experimentally and numerically. The tubes, manufactured in Cr alloy 718 (Inconel®), were smooth or with repeated rib-roughness (annular or helical ribs), and were tested at the solar furnace SF60 of the Plataforma Solar de Almería (PSA) in 2017 within the international access program of SFERA II project, financed by the EU. The specific focus of the tests was the assessment of the role of turbulence promoters in reducing the peak wall temperature when a strong one-side heating is present, contributing to the reduction of the thermal gradients between the irradiated and the non-irradiated (back) side of the tube. The experimental results show that the use of turbulence promoters reduce the wall temperature with respect to the case of a smooth tube, as expected, although the comparison between the samples is not trivial in view of the change in the optical properties induced by the progressive oxidation of the irradiated surface. Computational Fluid Dynamic (CFD) 3D models have been developed for the three samples and they have proven the capability to very-well reproduce the experimental results. A fair comparison between the different simulated tubes in the same controlled conditions of one-side heating has been performed numerically, assessing quantitatively the temperature reduction induced by the turbulence promoters, and the best performance of the Inconel® tube equipped with helices.

Keywords: Solar Tubular receivers, Turbulence promoters, One-side heating, CFD, TEF, Heat transfer enhancement.

Nomenclature

Symbols

A	area (m^2)
CD$_{\kappa\omega}$, D$_\omega$	cross diffusion terms (s^{-2})
d	distance to the wall (m)
D	diameter (m)
E	irradiated energy (Wh)
f	friction factor
F$_1$, F$_2$	blending functions
g	Earth's gravity acceleration (m/s^2)
Gr	Grashof number
HTC	Heat Transfer Coefficient (W/m^2/K)
k	thermal conductivity (W/m/K)
L	length (m)
Nu	Nusselt number
p	pressure (Pa)
P$_\kappa$	Production term for the turbulent kinetic energy (kg/m/s^2)
P$_\omega$	Production term for the specific dissipation rate (kg/m^3/s^2)
PF	proximity factor
Pr	Prandtl number
Q	heat flux exchanged between interfaces (W/m^2)
Ra	Rayleigh number
Re	Reynolds number
S$_\kappa$	Source term for the turbulent kinetic energy (kg/m/s^2)
S$_\omega$	Source term for the specific dissipation rate (kg/m^3/s^2)
T	temperature (K)
TEF	Thermal Enhancement Factor
v	velocity (m/s)
V	volume flowrate (l/min)
x, y, z	coordinate system

Greek symbols

α	absorptivity
β$_N$	thermal expansion coefficient (K^{-1})
β, β*	Turbulence model coefficients
Δp	pressure drop (Pa)
ε	emissivity
θ	local incident angle (°)
κ	turbulent kinetic energy (m^2/s^2)
μ	dynamic viscosity (Pa·s)
μ$_T$	Eddy viscosity (m^2/s)
ν	kinematic viscosity (m^2/s)
ρ	density (kg/m^3)

σ$_\kappa$, σ$_{\kappa 2}$, σ$_\omega$, σ$_{\omega 2}$	Turbulence model coefficients
σ$_x$, σ$_y$	standard deviation
φ	applied heat flux (W/m^2)
Φ	thermal power (W)
ω	specific dissipation rate of the turbulent kinetic energy (s^{-1})
ζ	Local coordinate along the wall-air interface, in the axial direction

Abbreviations

AMG	Algebraic Multigrid
CFD	Computational Fluid Dynamics
CIEMAT	Centro de Investigaciones Energéticas, Medioambientales y Tecnológicas
CSP	Concentrating Solar Power
DNI	Direct Normal Irradiance
GCI	Grid Convergence Index
IA	Inconel Annular
IH	Inconel Helices
IS	Inconel Smooth
PSA	Plataforma Solar de Almería
RANS	Reynolds-averaged Navier–Stokes
SFERA	Solar Facilities for the European Research Area
SST	Shear Stress Transport
TK	Thermocouple of the K-type

Subscripts

air	air
amb	ambient
base	baseline
bulk	bulk
cum	cumulated
ext	external air
i	internal
in	inlet
nconv	natural convection
o	at ambient conditions
out	outlet
peak	peak
s	smooth
S	surface
th	thermal
V	volume flowrate (l/min)
wall	wall
∞	outside the thermal boundary layer

1. Introduction

Context and background

The Concentrating Solar Power (CSP) technology includes systems used to generate electricity by the concentration of direct solar beam and the use of a conventional power block [1]. Among the other CSP systems, Solar Central Towers, with their single receiver placed on top of a tower surrounded by hundreds or even thousands of heliostats and very high concentration ratios [2], can reach higher temperatures and greater thermodynamic cycle efficiency than the other systems [3].

The 10 MW Solar One (1981) and Solar Two (1995), built in the Mojave Desert of California [4], were the first central receiver plants to be demonstrated. Other plants, such as the 11 MW PS10 and 20 MW PS20 in Spain, and the 5 MW Sierra Sun Tower in California were completed already 20 years ago [5].

The tubular external receiver technology is the most used in the central tower systems (although tubes are adopted also inside cavity receivers) [6]: the solar radiation reflected by the heliostat field is concentrated on the external surface of the absorber tubes and transferred to a working fluid flowing within them. The absorber tubes are exposed to strong one-side heating. On the external surface of the heated side of the tube, where the radiation absorption occurs, radiative and convective heat losses to the surrounding are remarkably high, given the high temperatures reached by the receiver [7], while on the corresponding inner surface heat is transferred to a working fluid. The non-heated side of the tube surface, in the lack of strong mixing of the coolant, typically lays at a temperature that is much lower than that of the heated side, generating strong thermal gradients. As high thermal stresses develop [8], tubular receivers are limited in the maximum heat flux that they can withstand. Moreover, the absorber tube lifetime is reduced by thermal fatigue, since the tubes are exposed to thermal cycles consisting of alternating heating and cooling processes related to daily switching on and off and variations in atmospheric conditions. The materials for the receiver are generally ceramics or metals since they need to be stable at relatively elevated temperatures.

The working fluid pumped inside the receiver tubes is heated up to produce electricity in the traditional power block. The choice of the heat transfer fluid depends on the plant design features, such as storage, loop configuration and hybridization. At the commercial level, tubular receivers adopt liquid heat transfer fluid, like water and molten salts [9]. Although the air thermal conductivity is low (it cannot be used to store directly the thermal energy), also the choice of pressurized air as heat transfer fluid could be widely justified by several advantages: it allows reaching very high temperatures and thus high efficiency of the thermodynamic cycle downstream the receiver; it can directly drive a Brayton cycle, which in turn allows adopting a highly efficient solar-driven combined cycle; it is for free and abundant and it has no risks of phase change. Tubular receivers operating with pressurized gases were used for example in the GAST [10], SOLHYCO [11] and SOLUGAS [12] projects.

Within the frame of the GAs-cooled Solar Tower project (GAST) project [10], different tubes (made by a nickel-iron-chromium alloy and by SiSiC, respectively) have been analyzed, with extensive material tests and thermo-mechanical analysis to investigate the effects of high-temperature operating conditions (~ 800 °C, increased to 1000 °C for the SiSiC tube). Within the SOLHYCO project [11] (developed in 2006-2010 at the Plataforma Solar de Almería), an innovative pressurized-air tubular receiver was designed, based on the "profiled multilayer tube" (PML) receiver concept. It was demonstrated that this technology enhances the heat transfer from the irradiated tube wall to the gas and allows to reduce the temperature

differences on the circumference of the tube, thus reducing stress and leading to higher lifetime. However, the different thermal expansion of Cr alloy 718 (Inconel® 718) and Copper led to progressive degradation of the inter-metallic connection, which dramatically reduced the lifetime of the component. The SOLUGAS project [12] consisted in the demonstration of the first solar hybrid power system with direct heating of pressurized air driven into a gas turbine at the MW scale; the solar receiver was made out of 170-nickel-alloy smooth tubes and heated pressurized air up to 800 °C.

The enhancement of the convective heat transfer to the pressurized air through turbulence promoters seems a clear direction to increase the maximum bearable heat load reducing the thermal stresses of the tubes subject to one-side heating. A wire-coil insert was already adopted in the tubes of the tubular air receiver in the SOLHYCO project [13]. From an experimental point of view, the enhancement of heat transfer and performance in a helically ribbed tube for a molten salt receiver, if compared to a smooth tube, was investigated in [14]. There, the authors used an electric heater mounted on the pipe, providing a uniform heat flux to the pipe, to demonstrate that the heat transfer of the helically ribbed tube was three times higher than that of the smooth pipe.

From a numerical point of view, the analysis of corrugated tubes, equipped with periodic rib-roughness such as helical ribs with different rib width and pitch, is already performed in [15]. After the calibration of the numerical model against experiments performed only in the case of a smooth pipe, the numerical model is extended to the cases of helical ribs without further validation, although the complexity of the thermal fluid dynamics is much higher. Nusselt number correlations are derived by imposing a uniform wall temperature as a thermal driver in all the simulations. Using the computed correlations within a system model, the authors could demonstrate that helical ribs are effective in reducing both the maximum and the average tube wall temperature, as already expected from the literature [16]. Note, however, that the numerical models for tubes equipped with helical ribs in [15] are not validated. Furthermore, the correlations derived for the corrugated tubes in the case of uniform heating on the tube surface are not straightforwardly applicable to the actual receiver conditions. This is due to the fact that the one-side heating drives an asymmetric development of the thermal boundary layer, which grows on the side of the tubes where the load is strongly concentrated, violating the symmetry assumption under which heat transfer correlations are typically derived.

On the pure modeling side, many efforts have been done by several authors to analyze the thermal performance of solar tubular receivers under steady-state and/or transient conditions using analytically, semi-empirical and numerical techniques, reviewed in [17]. Purely analytical models allow the quick estimation of the maximum tube temperatures, but they are unable to provide an accurate thermal profile over the full heat transfer surface. Semi-empirical models attempt to apply heat and mass balances to a reduced number of discrete nodal elements on the receiver surface, to evaluate the tube temperatures and receiver losses, without solving mass, momentum and energy conservation on a large fluid domain. That kind of models have been recently used to analyze the case of a liquid-sodium receiver: in [18], the performance of designs differing for size and connection of the pipes are compared, and in [19] a specific design of the receiver is analyzed, subject to different environmental conditions. There, a detailed (CFD) model is developed not for the coolant inside the smooth pipes, but rather for the external air flow, to compute the convective losses to the environment, as also done in [20]. In [21], the optimum heat transfer condition is investigated for a tubular type solar receiver for various receiver pipe sizes, heat transfer fluid (molten salt, sodium, and supercritical carbon dioxide sCO2) and design requirement and constraints. In [22], the energetic and exergetic performance of different heat transfer fluids, including ideal air, is

investigated in a tubular receiver model, allowing the identification of the irreversibility associated with the various heat transfer processes occurring in the receiver pipes. Note, however, that all the above-mentioned applications require constitutive relations for the heat transfer to the coolant. Standard smooth-pipe correlations for heat transfer *with azimuthally uniform heating* are typically used, without an assessment of the validity of those correlations in the peculiar case of one-side heating. An assessment in that direction comes from the study in [23], related to the nuclear field rather than to CSP, where it is shown that the Sieder-Tate correlation [24] can reproduce the heat transfer occurring in pipes with water in forced flow, subject to strong one-side heating, with only a rough approximation. That result highlights the need for dedicated analysis on the heat transfer in situations where the heat load is azimuthally strongly non-uniform.

As a matter of fact, the one-side heating inside smooth tubes has been analyzed by several authors with numerical CFD models that require a significant computational effort to solve the conjugate heat transfer problem in the internal flow and in the tube wall. The numerical analyses found in literature span from the very computationally-intensive Direct Numerical simulations (DNS), like the one reported in [25] for a tube of a solar receiver, to more standard Average-Navier-Stokes (RANS) approach. Both are, however, hardly usable if every single tube of a whole tubular receiver has to be simulated, calling for a multiscale approach, as already adopted for open volumetric air receivers in [19]. With much simpler models, the numerical investigation of the efficiency of the heat transfer to the fluid, for a smooth pipe in an external receiver under unilateral concentrated solar radiation was carried out in [26], for different values of the energy flux incident on the tube. The analysis in [27] demonstrated that a model accounting for the azimuthal variation of the heat flux leads to a higher maximum wall temperature, which is the critical point for the molten salt receiver analyzed there. Again, the analysis there is performed on a smooth tube. The authors concluded that an appropriate tubular receiver design must account for the azimuthal temperature variation in the pipe, so for the one-side heating of the tubes. In [28], a thermal analysis of thin-wall pipes under non-uniform heat flux in the azimuthal direction, with turbulent flow in statistically-stationary-state, is presented, but again the tubes are not equipped with any turbulence promoter.

Aim and novelty of the work

As shown above, in the literature one can find analyses of smooth tubes, which are subject to one-side heating but which are not equipped with turbulence promoters, or analyses of tubes equipped with turbulence promoters, but exposed to uniform heating, where the thermal boundary layer develops in an axisymmetric way. No experimental nor numerical studies are available for tubes equipped with periodic rib-roughness turbulence promoters, subject to strong one-side heating, where the asymmetry in the thermal boundary layer development makes the standard uniform-heating correlations of doubtful value.

In the present paper, we aim indeed at bridging some of the gaps in the comparative assessment of the thermal performance of tubular receivers equipped with turbulence promoters when subject to one-side heating. We investigated experimentally and numerically the thermal behavior of three monolayer absorber tubes, equal for material but different for turbulence promoter configuration, heated in a solar furnace, following two parallel directions:

1. For the first time, three Inconel® 718 tubes samples (a smooth tube, and two samples equipped with periodic rib-roughness turbulence promoters, and namely a tube equipped with annular ribs and a tube equipped with helical ribs) have been tested under the same conditions of one-side heat flux within a solar furnace as tubular receivers. The test campaign, performed at the solar

furnace SF60 [29] located at the Plataforma Solar de Almería (PSA) [30] in 2017 within the international access program of SFERA II project [31], financed by the EU, aimed at assessing if a clear increase of performance could be measured moving from the smooth tube to the sample with annular ribs and to that with helical ribs.

2. For the first time, a CFD model considering one-side heating as a thermal driver is developed not only for a smooth tube, but also for tubes with annular and helical turbulence promoters. The CFD model for all three samples has been validated against the experimental data collected in the experimental campaign within the solar field. The model proves the capability to reproduce the effects of the turbulence promoters when the thermal driver is strongly non-uniform in the azimuthal direction.

The model of the corrugated tubes, once validated, is then exploited in the paper to perform a comparison between the thermal-hydraulic performance of the three tubes *when the same heat flux, oxidation level and fluid flow are considered*. The comparison, which could not be performed in such fair form in the experiment, allows assessing *quantitatively* the better performance of the tubes equipped with turbulence promoters.

The paper is organized as follows: the three tube samples are described in Section 2. In section 3, the data collected during the experimental campaign are first critically evaluated, then the test results are presented and discussed, highlighting the need for computational analysis. In Section 4, the CFD models developed for the different tubes are presented, verified, calibrated and validated against different sets of experimental data. In Section 5, a detailed comparison between the thermal-hydraulic performance of the different tubes for the same controlled load condition is performed, both in terms of pure *thermal* performance and in terms of thermal enhancement factor, which also includes the *hydraulic* performance (pressure drop). The conclusions of the analysis are given in Section 6.

2. The samples

The three tubes, manufactured within the present work through additive manufacturing (3D printing), have the features reported in Table 1.

Table 1 – Main features of the sample absorber tubes manufactured and tested at PSA in 2017.

Tube label	Turbulence promoter	Length (mm)	Diameter (mm)	Wall thick. (mm)
IS	None (smooth)			
IH	Helical ribs	250	25.4	2.4
IA	Annular			

All tubes are made of Inconel® 718, including a smooth one (IS) which should be the bottom-line reference. As turbulence promoters, we targeted repeated rib-roughness tubes, and in particular annular and helical ribs, which seemed easy to manufacture at a reasonable cost, and for which guidelines for the

optimization were already present in literature [32], although referring to cases of uniform heat flux. For the pipe equipped with annular ribs, the pitch, width and height of the ribs were designed to 6 mm, 1 mm and 1 mm, respectively, to maximize the heat transfer coefficient based on a preliminary and simplified CFD study, where the computed heat transfer increased for increasing pitch/height ratios up to 5 and then flattened out for values of pitch/height ratios up to 7 (the largest value numerically tested). However, due to manufacturing issues in controlling the backward shape of the ribs, they resulted in having a trapezoidal shape, instead of the original rectangular design, with an angle of attack of 90° in the flow direction and of 45° in the other direction.
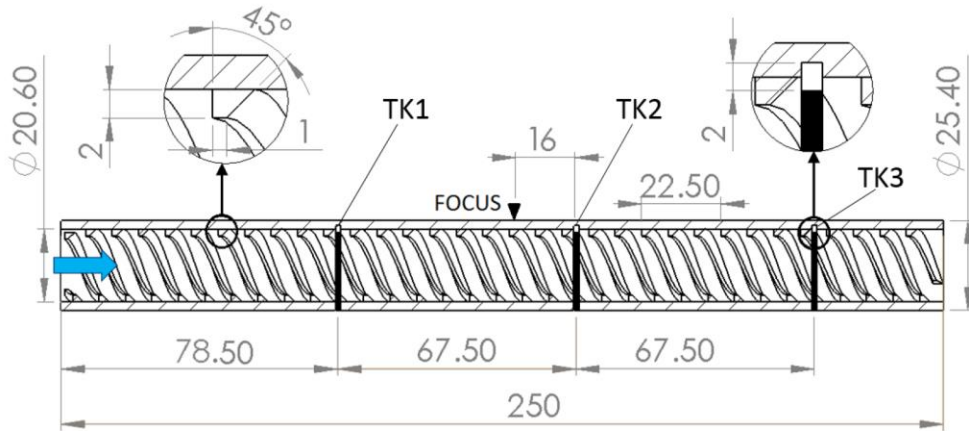
(a)

(b)

Figure 1 – (a) Drawing of the helically ribbed tube. All the quotes are expressed in [mm]. (b) Picture of one of the Inconel® tubes before the test campaign with the supports for the thermocouples (the squares in the background have 1 cm side).

The helical-ribbed tube (IH) was originally designed with helices, having a rectangular shape with an aspect ratio of 2, with the pitch of 22.5 mm (resulting again from a preliminary and simplified CFD optimization of the heat transfer). Note that the number of threads (three) came out to give a longitudinal distance between the ribs comparable to the rib pitch in the IA tube. Due again to manufacturing constraints, the original design was slightly changed: also the helical ribs have a trapezoidal shape, as shown in the left-zoom in Figure 1a, with an angle of attack of 90° in the flow direction, a width of 1 mm and an angle of attack of 45° in the other direction. All the geometric details of the IH configuration as manufactured are provided in Figure 1a. A comparative picture of the cross-sections of the IA and IH tubes is provided in

Figure 2, where the different height of the ribs in the two tubes is evident. Since the manufacturing was taking longer than foreseen, the tubes were left "naked" as shown in Figure 2, without any coating or painting on the external surface because of lack of time. *A posteriori*, the benefit of applying a painting with controlled emissivity should have been considered with much more attention, since the interpretation of the experimental results resulted to be strongly affected by the surface oxidation, see below.

In view of the tests at the PSA, three holes were drilled in the tubes by the manufacturer, to insert three thermocouples of the K-type from the back side (the not irradiated one) into the front wall (the irradiated one), close to the external surface. These thermocouples were not welded and were partially inserted by 1 mm inside the inner front wall thanks to pre-formed holes. The nominal position of the focus point is shown in Figure 1a, but it can slightly change in a non-controlled way during the tests, due to small variations of the heliostat position, see below.
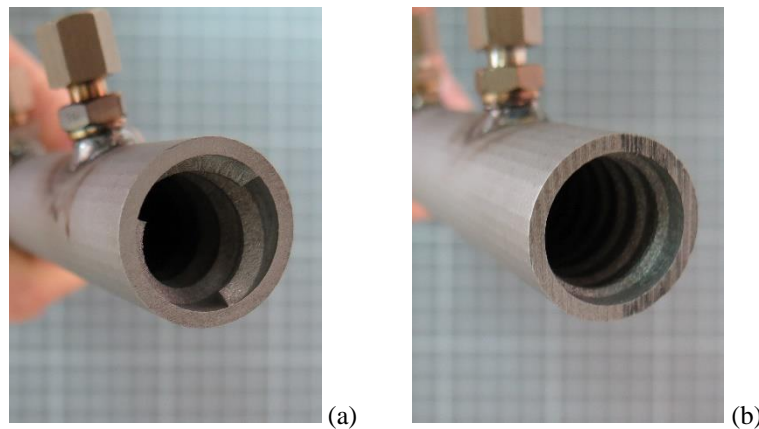

(a)   (b)

Figure 2 - Detail of the Inconel® tube equipped with helical ribs (a) and annular rings (b), respectively.

3. Tests

3.1 Test setup

The PSA, the largest of its kind in Europe, is owned and operated by the Spanish Research Institution CIEMAT. It has been exploited in Andalusia since 1980 for the testing and optimization of a variety of high-temperature solar technologies [30]. In the R&D unit devoted to the Solar Concentrating Systems, the 0.6 MW$_{th}$ High-Flux Solar Furnace (SF60) operates since 1991. It consists of a flat collector mirror, or heliostat (with a surface of 140 m^2), reflecting the parallel horizontal solar beams on the parabolic dish, which in turn reflects them on the test sample focus, see Figure 3a. The amount of incident radiation is regulated by the shutter located between the concentrator and the heliostat. A test table movable in three directions (East-West, North-South, up and down) places the test samples in the focus with great precision. When the shutter is completely open with a Direct Normal Irradiance (DNI) of 1000 W/m^2, the peak irradiance at the focus is about 3 MW/m^2 and the total power is 69 kW. The power focal diameter is 26.2 cm [33].

(a)   (b)
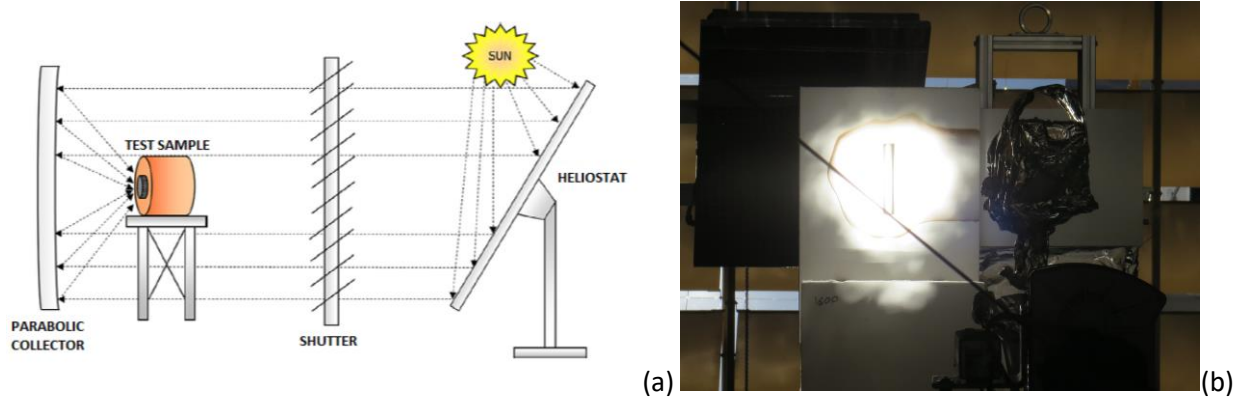
Figure 3 – (a) PSA Solar Furnace working sketch, according to [33]; (b) Alumina sheet to protect the connections to the sample.

The samples were mounted on the testbed and they were connected in parallel branches to the air distribution system (see the sketch in Figure 4) through a couple of nuts mounted on the sample tube ends, which reduced the irradiated length from the original ~250 mm to about ~210 mm. The nuts, as well as the rest of the air circuit, were protected against the concentrated solar radiation by means of an alumina sheet placed in front of the testbed. A hole in the alumina plate allowed to focus the concentrating solar power just on the sample tube (see Figure 3b). The amplitude of the peak of the Gaussian distribution was measured by means of a radiometer, which had to be placed in the focus replacing the test sample. For this reason, the tube samples could not be tested while the heat flux was being monitored and the incident radiation was measured before/after each test. A 7.5 kW compressor increases the pressure of ambient air up to 10 bar (absolute pressure): the air passed through the tube(s), removing heat, and then was cooled down in a water heat exchanger, before being released to the ambient. The flow rate was measured, and it could be regulated through a valve positioned upstream of the sample.
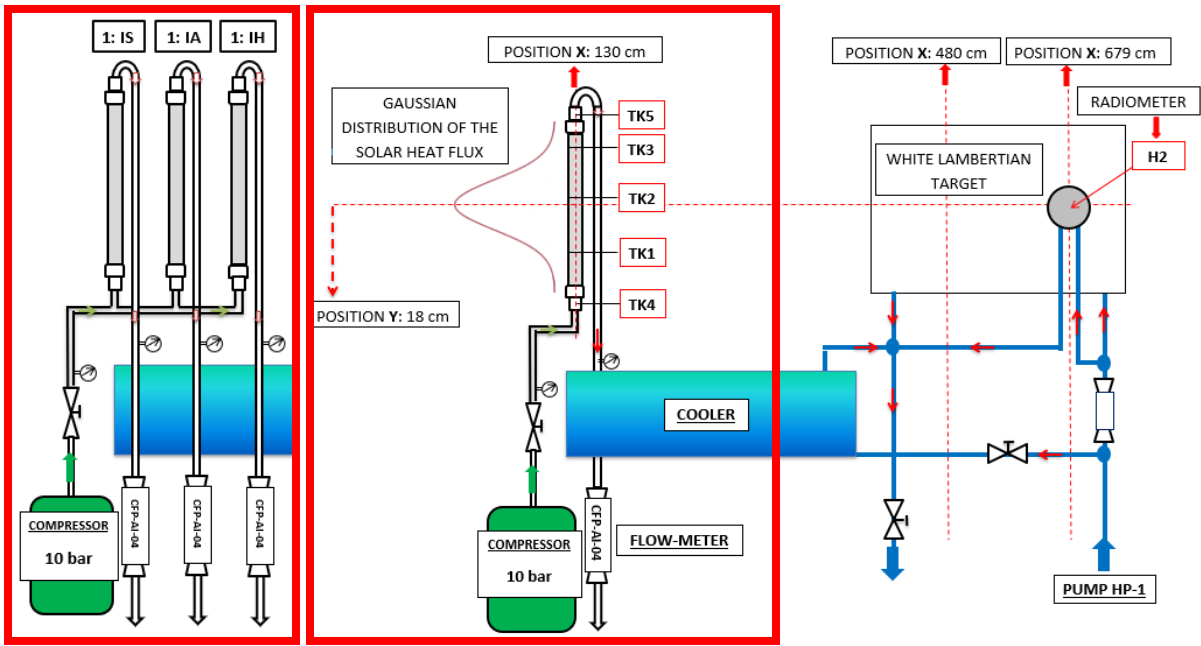

Figure 4 – Sketch of the hydraulic circuit where samples were inserted for the tests at the PSA. The two portions of the circuit in the red rectangle, with 3 or 1 sample installed at the same time, were tested alternatively.

9

The available instrumentation was constituted by:

- Thermocouples of the K-type for the temperatures, with an accuracy of ± 1.5 K. The thermocouple wires are protected from the surrounding ambient by a sealed stainless-steel sheath. Their location for all the samples is reported in Figure 1a and in Figure 5a. As already mentioned above, the thermocouples TK1, TK2 and TK3 in each sample were not welded but just put in contact with the pipe in the pilot holes pre-arranged during the tube manufacturing. The 2-mm-long tips of thermocouple were partially inserted into the pre-formed hole in the tube wall (1 mm), and partially exposed to air (1 mm), so that they measured an air/wall average temperature in the proximity of the inner surface of the tube. The thermocouple TK4 is to confirm that the air inlet temperature is the ambient one, which is also provided by the PSA control panels. The thermocouple TK6 measures the air temperature at the flow meter position. Since the air density is a function of the temperature, the mass flow rate can be determined by coupling the TK6 and the flow meter readings. The thermocouple TK5, which should measure the air mean temperature at the outlet of the tube sample, allowing estimating the useful power transferred to the fluid by calorimetry, was unfortunately not well positioned in the core flow or it bended, so that its read-out was considered not reliable and discarded in what follows.
- Radiometer for the peak heat flux in (kW/m^2). To measure the peak heat flux, the target in the focus of the parabolic collector was moved from the sample to a Lambertian target, see Figure 4, by means of the movement of the mobile test-bed. The radiometer adopted at the SF60 is affected by a systematic error that depends on the spectral absorptivity of the black coating of the sensitive part (made of colloidal graphite) and results in an overestimated heat flux. To take that error into account, a correction factor of 0.782 was determined in [34]. The amplitude of the peak of the Gaussian distribution has an accuracy of ±3%, according to [34]. The incident heat flux can be then calculated according to the Gaussian distribution defined in [33] and reported in Eq.1, where the cosine of the local incident angle is inserted to take into account the curvature of the tube surface. The reference system is shown in the top view section of Figure 5b: the local incident angle can be evaluated through simple trigonometry, while the z-origin is positioned in correspondence to the focal point so that the peak of the heat flux is obtained for x = z = θ = 0.

$$\varphi = \varphi_{peak} \cdot \left\{ exp\left[-\frac{1}{2} \cdot \left(\frac{x^2}{\sigma_x^2} + \frac{z^2}{\sigma_z^2} \right) \right] \right\} \cdot \cos\theta \qquad \text{(Eq.1)}$$

In Eq.1, σ_x and σ_z are the standard deviations, both equal to 0.064 [33]. We neglect the other possible sources of inaccuracies, and namely the fact that the peak load could change while the measurement panel shifts from the sample to the radiometer, and the fact that the local focus of the flux on the sample could be instantaneously in a different position, as the heliostat, tracking the sun, is moved by the wind coming from any possible direction.
- Flow meter with an integrated control system (Bronkhorst High-Tech model F-203AV Mass Flow Controllers, well suited for gases), to measure and control the flowrate in (l/min). The stated accuracy of the sensor [35] is of ± 0.5% of the actual flow rate reading, plus a ± 0.1% of the full scale of the instrument (1650 l/min in this specific case); additionally, another ± 0.1% of the full-scale error has still to be added due to some uncertainty related to the control stability.
- Pressure switch, for the control of the pressure at the outlet of the compressor, i.e., the air inlet pressure in the sample, measured in (bar);

- Pyrheliometer, for the instantaneous DNI in (W/m^2), to check if the operation could start;
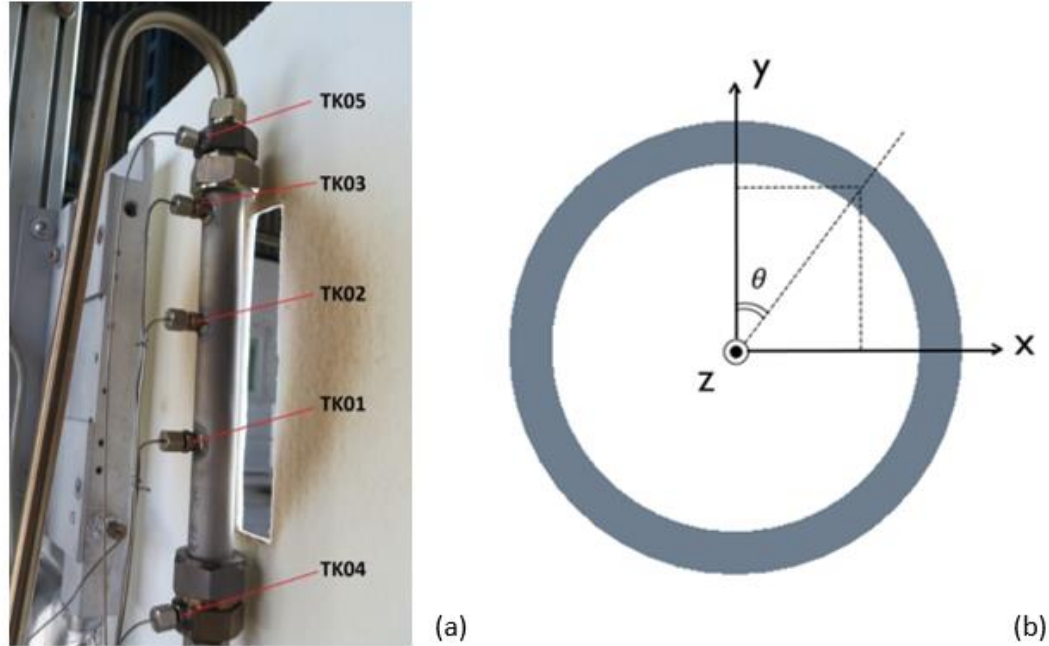

Figure 5 – (a) Connection of one sample to the hydraulic circuit, with the location of the different thermocouples; (b) top view of the tube section and reference coordinate system.

3.2 Test results

During the two weeks of experimental campaign transient and "quasi" steady-state tests were performed, but the formers are not analyzed in this paper.

Steady-state tests aim at obtaining equilibrium between the power applied to the sample, the thermal losses and the useful power to the fluid. Because of the intrinsic variability of the solar heat source, strictly speaking, only "quasi" steady-state tests can be performed, obtained regulating the shutter to have the desired peak heat flux. When the heat flux seemed quasi-steady from the radiometer measurement, the mobile test bed was moved to shine on the receiver. The measurement was carried on until all the temperature traces got to a quasi-steady state (at least for a couple of minutes), then, to conclude the test, the radiometer was positioned a second time in the focus to measure the peak heat flux to be compared with the initial one, to check that no significant variations occurred.

For all the tests considered here, in order to consider them "steady", we allowed a maximum variation of the measured temperatures, as well as of the peak heat flux, of ±3% (i.e., equal to the major instrumentation error, see below). The wind velocity safety limit was 30-35 km/h, as a larger wind velocity would force to move back the heliostat in the horizontal position (and stop the tests). A summary of all the steady-state tests considered in the present analysis is reported in Table 2. For all samples, three peak flux levels (~55 kW/m^2, ~180 kW/m^2 and ~280 kW/m^2, respectively) were tested, while the flow rate was kept constant in almost all the tests (~40 l/min). Also, Table 2 shows the experimental data of the three thermocouples for the inner wall temperature and the read-out of a thermocouple measuring the ambient temperature.

In addition, for every test performed during the experimental campaign (both steady-state and transient), an average peak heat flux was extracted from the radiometer output (W/m^2); the Gaussian

11

distribution given by this peak was then integrated on the irradiated surface of the tube (W) and multiplied by the irradiation duration, to obtain a "cumulated irradiated energy" (E_{cum}, in [Wh]) on each sample. E_{cum} indicates how much each sample has been exposed to concentrated solar power. The very first test on each sample is, by definition, in "as-received" conditions, which means that the component had never been irradiated yet so that E_{cum} was zero. Note that the IH tube was already significantly irradiated before the three tests analyzed here and reported in Table 2.

Table 2 - Summary of all the quasi-steady state tests considered in the present analysis.

Sample	Date	Test ID	Heat Flux (kW/m²)	V (l/min)	TK01 (K)	TK02 (K)	TK03 (K)	T_{amb} (K)	E_{cum} (Wh)
IS	19/09/2017	IS1	180.9	40	492.9	600.6	447.1	300.5	0
		IS2	63.5	25	380.9	450.6	360.8	303.1	564.8
	25/09/2017	IS3	54.7	40.5	358.4	464.7	353.2	300.1	716.9
		IS4	177.7	40.5	489.3	683.3	482.8	301.1	760.9
		IS5	266.7	41.5	600.6	797.3	563.4	305.4	824.8
IA	22/09/2017	IA1	53.8	38.2	346.3	397.6	360.2	297.2	0
		IA2	190.1	39.5	502.9	594.9	501.8	297.9	95.8
	25/09/2017	IA3	54.6	39.5	379.8	446.7	376.1	295.8	463.9
		IA4	177.8	40.5	490.3	625.5	512.9	302.3	513.1
		IA5	279.3	40.5	535.8	754.7	614.4	303.4	582.1
IH	25/09/2017	IH3	54.6	39.5	350.5	418.2	378.1	299.3	1187.2
		IH4	182.9	39.5	448.0	622.0	538.4	303.6	1201.2
		IH5	279.3	41.5	547.5	765.9	629.9	302.8	1256.2

Oxidation

As mentioned above, the samples were manufactured using additive manufacturing, but no surface coating was applied to them. This means that high concentrated heat flux can alter the wall surface properties by oxidizing it. In particular, both emissivity ε and absorptivity α can be affected by the oxidation level [36] . When the absorption factor increases, the amount of Sun power entering the system increases. For this reason, an analysis of the sample behavior in very similar conditions was carried out, but in different days: as expected, the temperature results higher in the last tests, when oxidation already occurred, as shown in Figure 6 the issue of emissivity and absorptivity will be specifically addressed in Section 4.

Note that, in Figure 6, the difference between the IS and IA curves at comparable heat flux can be attributed to the effect of the turbulence promoter in the IA tube. The two different curves for the IA samples, instead, reach different temperature levels because of the different heat flux level. While the increase of TK2 when comparing IA3 to IA1 can be only attributed to the increase in the oxidation level for the IA3 test, the much smaller increase of the TK2 value when comparing IA4 to IA2 hides a counteracting effect of the heat load, which is slightly higher in IA2 than in IA4.
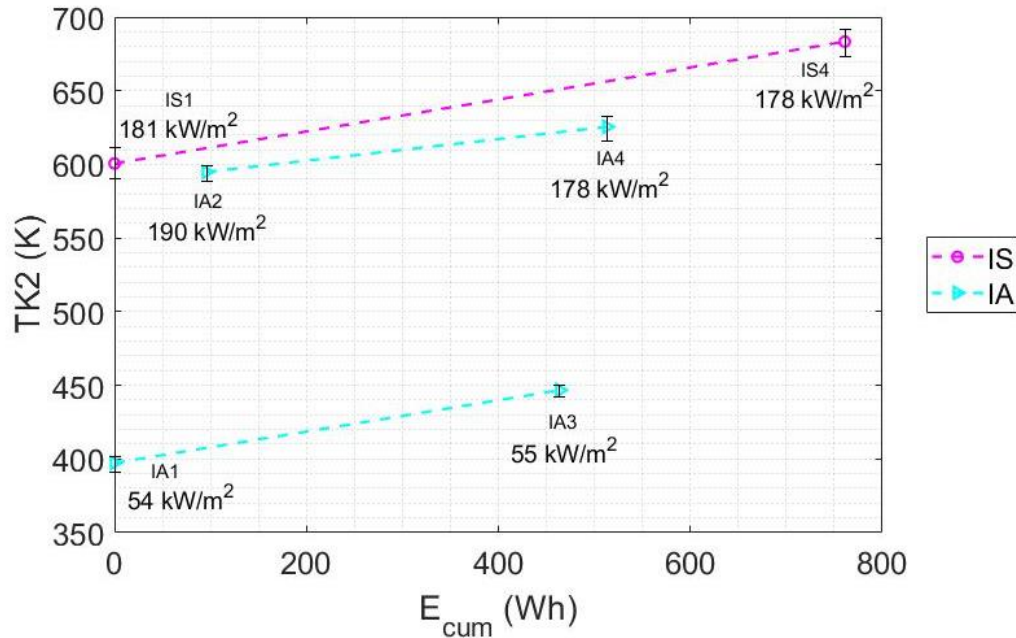
Figure 6 - Measured temperatures in TK2 for different samples, in couples of tests performed in similar heat flux conditions, but on different days (reported in the labels).

The evidence of the oxidation will be relevant for the CFD analysis settings, see below, and only a proper modeling of the effects of the oxidation on the emissivity and absorptivity will allow a fair comparison between the test results.

Inner wall temperature

The first comparison between the three tubes could be done in terms of TK2 peak value, where the maximum temperature among the three different positions along the tube axis is expected, as TK2 is the thermocouple located closer to the focus of the parabolic collector, see Figure 1a. The comparison is reported in Figure 7, showing, however, that it is not possible to draw conclusive statement: for example, depending on the case, the IH tube shows either larger and smaller temperatures with respect to the IA tube ones.

The comparison of the thermal performance of the different tubes is not straightforward since the large variation of the optical properties in time affects them. Tests on different tubes for a similar level of cumulative incident power are present in the database, but unfortunately not at a comparable solar incident flux, so that a direct comparison only based on the experimental results would not be correct: only a proper numerical modeling could allow a fair comparison between the different configurations.
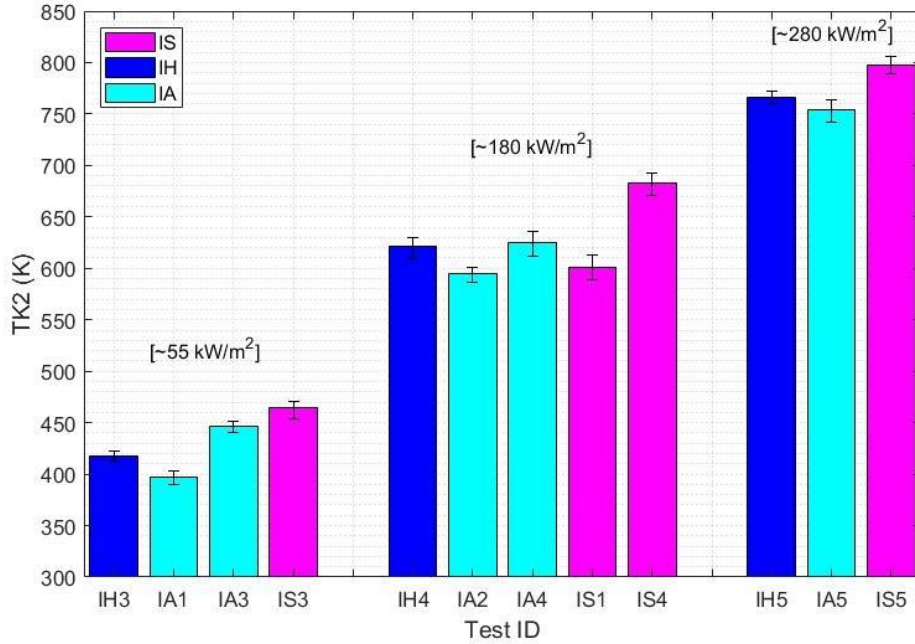
Figure 7 - Measured peak temperature (TK2) for different heat flux levels on the different samples, at almost equal flowrate (40 l/min).

4. CFD modeling

4.1 Model and simulation setup

In this work, the 3D CFD steady-state conjugate heat-transfer problem with non-uniform heat flux in both azimuthal and axial directions has been addressed using the commercial software STAR-CCM+ (version 13.02.013-R8), which implements a cell-centered Finite Volume method. The computational domain includes the solid and fluid regions of the irradiated samples, as well as the three thermocouples inserted in the wall.

A two-equation Reynolds-averaged Navier–Stokes (RANS) turbulence closure [37], and namely the SST-Menter $\kappa{-}\omega$ [38], was selected here to compute the turbulent or eddy viscosity μ_T, with an all-y+ treatment at the wall. The two transport equations, one for the kinetic energy κ and another for the specific dissipation rate ω, added to the standard RANS in the SST-Menter $\kappa{-}\omega$ model, are reported in Eqs.2-3[1].

$$\frac{\partial}{\partial t}(\rho\kappa) + \nabla\cdot(\rho\kappa\bar{\mathbf{v}}) = \nabla\cdot[(\mu + \sigma_\kappa\mu_T)\nabla\kappa] + P_\kappa - \rho\beta^*(\omega\kappa - \omega_0\kappa_0) + S_\kappa \qquad \text{(Eq. 2)}$$

$$\frac{\partial}{\partial t}(\rho\omega) + \nabla\cdot(\rho\omega\bar{\mathbf{v}}) = \nabla\cdot[(\mu + \sigma_\omega\mu_T)\nabla\omega] + P_\omega - \rho\beta(\omega^2 - \omega_0{}^2) + S_\omega \qquad \text{(Eq. 3)}$$

where ρ is the fluid density, $\bar{\mathbf{v}}$ is the mean velocity, μ the dynamic viscosity, σ_κ and σ_ω are coefficients of the model, set to 0.85 and 0.5 respectively, β^* and β are model coefficients [38], see below, κ_0 and ω_0 are

---

[1] Modification factors accounting for free-shear and/or vortex shredding are neglected here.

14

the ambient turbulence values, to counteract the turbulence decay, P_κ and P_ω are the production terms for κ and ω, respectively, and S_κ and S_ω are the source terms.

It is well known that the κ–ε model, which adds to the RANS equation two transport equations, one for κ and another for its dissipation rate ε, respectively, is unsatisfactory in predicting separating and rotating flows in the near wall region, resulting in an overestimation of turbulent kinetic energy and turbulent viscosity; this is mainly due to the empirical nature of the constants used in the equation for ε [39]. On the other hand, the standard κ–ω model, which adds a transport equation for the turbulent frequency ω, rather than for ε, has improved performance in modeling the boundary layers under adverse pressure gradients, which is a critical feature of the case under study: indeed, the turbulence promoters are designed specially to provide recirculation and rotating flows, to enhance the heat transfer. Nevertheless, boundary layer computations are sensitive to ω values in the core stream, problem that does not occur for the modeling with the κ–ε model. The selected SST-Menter κ–ω model is able to work as a standard κ–ω model in the near wall region, and as the κ–ε model in the fully turbulent region, through a blending function, which adds a cross-diffusion term, activated only in the main stream. The blending function is hidden in the production term P_ω for ω, which accounts for an additional cross diffusion term D_ω if compared to the standard κ–ω model, see Eq.4.

$$D_\omega = 2\rho(1 - F_1)\sigma_{\omega 2}\frac{1}{\omega}\nabla\kappa \cdot \nabla\omega \qquad \text{(Eq. 4)}$$

In Eq.4, $\sigma_{\omega 2}$ is set by default to 0.856, and F_1 is the blending function defined in Eq.5, which depends on the distance to the wall d and contains a proximity factor PF (Eq.6) and a cross diffusion term $CD_{\kappa\omega}$ (Eq.7) allowing the model to blend to a κ–ε model far from the wall.

$$F_1 = tanh\left(\left[min\left(PF, \frac{2\kappa}{d^2 CD_{\kappa\omega}}\right)\right]^4\right) \qquad \text{(Eq. 5)}$$

$$PF = \max\left(\frac{\sqrt{\kappa}}{0.09\omega d}, \frac{500\nu}{d^2\omega}\right) \qquad \text{(Eq. 6)}$$

$$CD_{\kappa\omega} = \max\left(\frac{1}{\omega}\nabla\kappa \cdot \nabla\omega, 10^{-20}\right) \qquad \text{(Eq. 7)}$$

Note that in Eqs. 2 and 3, β^* is a constant, set to 0.09, while β depends linearly on F_1, as set in Eq.8.

$$\beta = -0.0078F_1 + 0.0828 \qquad \text{(Eq. 8)}$$

The production terms for κ, P_κ adds, to that of the standard κ–ω model, an additional non-linear term, accounting for the anisotropy of turbulence as a quadratic dependence between the strain and vorticity tensors. That substitutes the linear relation between the stress tensor and the mean strain rate, used in the standard RANS κ–ε and κ–ω models in the Boussinesq approximation of the Reynolds stresses.

In the SST-Menter κ–ω model, the turbulent kinematic viscosity is defined as the product of κ by a timescale τ which is not straightforwardly the reciprocal of ω, as in the standard κ–ω model, but it hides in Eq.9 a second blending function F_2, defined in Eq. 10 as a function of the distance to the wall.

$$\tau = min\left(\frac{1}{\omega}, \frac{0.31}{S \cdot F_2}\right) \qquad \text{(Eq. 9)}$$

$$F_2 = tanh([PF]^2) \qquad \text{(Eq. 10)}$$

A second order upwind scheme was chosen to discretize the advection terms. A segregated flow solver was chosen, which uses an Algebraic Multigrid (AMG) method to reduce efficiently the numerical error in the iterative solution. A segregated fluid temperature model was selected to solve the energy conservation.

For the fluid region, the air in turbulent flow is compressible and its conductivity, specific heat and viscosity are considered as functions of the fluid temperature, reproducing the data from [24]. The air density is computed according to the state equation for an ideal gas, embedded in the software, while the Pr number, being almost constant, is directly set equal to 0.7.

For the solid region, the properties of Inconel® 718 have been set, with specific heat capacity and thermal conductivity taken as polynomial functions of the temperature.

The domain shown in Figure 8 is the one used for the IS and IA models: thanks to symmetry in the geometry, as well as in the thermal driver and boundary conditions, it is possible to reduce the computed domain to half. For the IH sample, the entire domain has been considered.
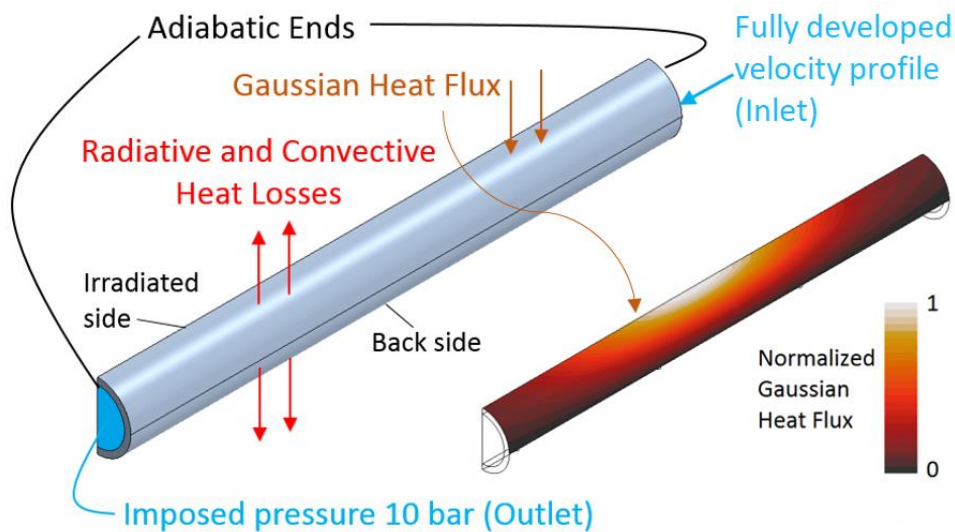
Figure 8 - Boundary conditions applied and normalized Gaussian heat flux distribution.

The following boundary conditions have been applied to the simulated tubes, as shown in Figure 8:

- Fully developed velocity profile at the inlet section, since a relatively long and straight pipe connects the tube sample inlet with the rest of the air circuit.

- Outlet pressure p_{out} = 10 bar applied as a uniform condition on the outlet cross section.

- Inlet air temperature T_{in} = 300K.

- For the turbulent equations, the turbulence intensity $v'/\bar{v}$, which is a measure of the root mean square of the local velocity fluctuations relative to the mean velocity, is set to the default value of 0.01 and the turbulent viscosity ratio μ_T/μ to the default value of 10 at the fluid boundaries.

- The axial boundaries of the solid tube are considered adiabatic. As conduction typically accounts for a very small fraction of the total heat losses from a receiver [40], it is common for heat transfer models in literature to treat conduction losses as negligible.

- For what concerns the driver of the simulations, i.e. the imposed heat flux, it is the same for all the models and the Gaussian distribution is a peculiar feature provided by the PSA. In literature, many different ways to set the solar heat flux have been found as: axial uniform heat flux [41], circumferentially varying heat flux [42] and non-uniform heat flux [28]. Here it is possible to set a very detailed solar heat flux because the CFD analysis is focused on the single tube. Note that this is typically not possible when moving to the full receiver level, due to the computational cost of the scaling-up. The Gaussian Solar Heat Flux is then applied to the irradiated side (see Figure 8) of the tube, with the distribution as in Eq.1: the peak flux ranged from ~50 kW/m^2 up to ~300 kW/m^2, depending on the selected test.

- Convective Heat losses towards the environment by free convection, applied to the external surface of the tube facing the open environment. The convective losses are computed according to the Newton's cooling law, as a function of the wall surface temperature (computed by CFD), the ambient temperature and the heat transfer coefficient. The ambient temperature was monitored during the test sessions, as shown in Table 2, while the heat transfer coefficient has been estimated using the empirical correlation in Eq.11 [43] :

$$Nu = \left[0.825 + \frac{0.387 \cdot Ra^{1/6}}{\left[1 + \left(0.492/Pr\right)^{9/16}\right]^{8/27}}\right]^2 \qquad (Eq.\,11)$$

In Eq.11, the Prandtl number Pr and the Nusselt number Nu, the latter evaluated using the tube length L as characteristic length, are evaluated at the ambient temperature T_∞. The correlation is for natural convection (as the test bed is protected from the wind) in laminar flow (Rayleigh number Ra, given in Eq.4, < 10^9), as in the cases examined here; however, it was developed for isothermal vertical planes, while our sample is a tube with a non-uniform temperature distribution. The resulting heat transfer coefficient varies case by case, as Ra depends also on the external surface temperature of the tube, as it is a function of the Grashof number (Eqs.12-13):

$$Ra = Gr \cdot Pr \qquad (Eq.\,12)$$

$$Gr = \frac{gL^3 \beta_N (T_s - T_\infty)}{v_{air}^2} \qquad (Eq.\,13)$$

where g is the standard gravity acceleration, L is the length of the pipe, β_N is the thermal expansion factor, v_{air} is the kinematic viscosity and T$_S$ is the mean surface temperature of the plate (tube surface). According to Eq.14, it is expected to have a relative higher heat transfer coefficient HTC_{nconv} (defined in Eq.14) in the case of higher peak fluxes (larger temperatures, returning larger Nu), namely in the range of 5-15 W/(m^{2}K).

$$HTC_{nconv} = \frac{Nu \cdot k_{ext}}{L} \qquad (Eq.\,14)$$

17

In Eq.14, k_{ext} is the thermal conductivity of the external air, computed at T_∞.
The convective heat losses can be then evaluated through the Newton's cooling law, in Eq.15, where the integral extends to all the external surface of the tube:

$$\Phi_{nconv} = HTC_{nconv} \cdot \iint (T_s - T_\infty) \ dA \qquad (Eq.15)$$

- Radiative Heat losses, computed according to the Stefan-Boltzmann's law, based again on the computed wall surface temperature. The latter requires defining the emissivity of Inconel® 718, which may range from about 0.2 to more than 0.9 depending on the oxidation grade [36] . Figure 9 shows the emissivity vs surface temperature for the Inconel® 718 in "as-received" conditions well reproduced by the fit in Eq.16 [36], where T_S is the surface temperature of the pipe, in Kelvin.

$$\varepsilon \ (T_s) = 1.12 \cdot 10^{-4} \cdot T_s + 0.213 \qquad (Eq.16)$$

Figure 9 shows a moderately low emissivity, which increases from a value of approximately 0.24 at a surface temperature of 200 °C to 0.33 at a temperature of 1000 °C. For the current work, the back wall of each pipe is always considered a not-oxidized surface, so that Eq.16 can be directly applied to compute the local value of the emissivity.

(a)

(b)
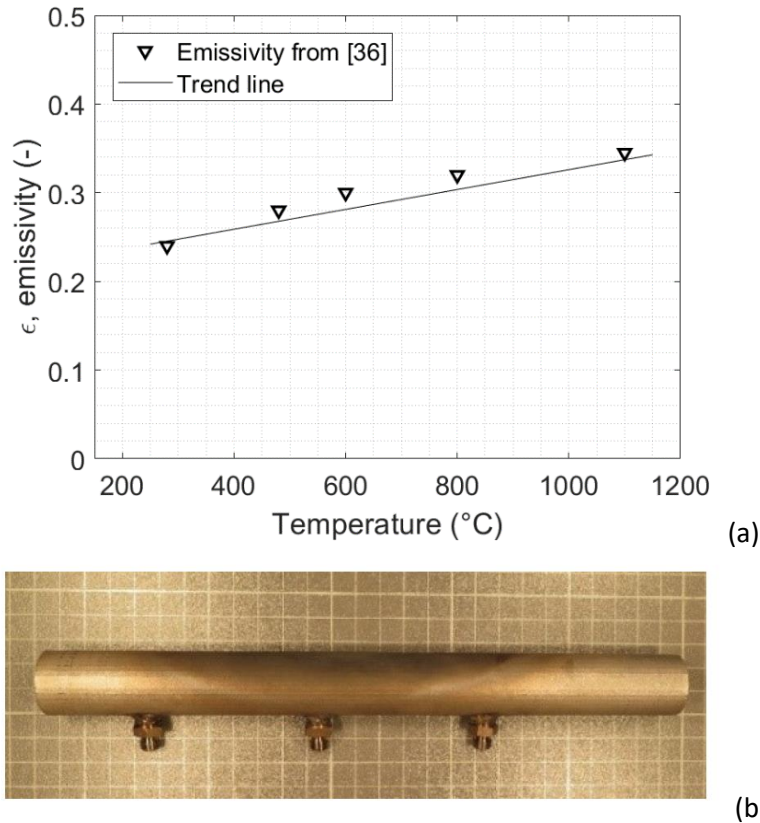
Figure 9 – (a) Emissivity vs sample temperature for Inconel® 718 in "as-received" condition [36], together with the trend line in Eq.16; (b) An oxidized sample tube after the test.

As no surface coating was unfortunately applied to the tube surface, oxidation occurred (as discussed above) leading to higher emissivity and absorption factors. In particular, the emissivity cannot be assumed uniform on the tube surface since it strongly depends on temperature. A good approximation is that the distribution of the surface emissivity on the irradiated wall has a Gaussian shape, which reflects the thermal driver. Since the temperature relevant to enter Figure 9a is the surface temperature, which has not been directly measured, the amplitude of the Gaussian distribution could be found only through a calibration procedure, see below.

The iterative solution of the conjugate problem is stopped when the residuals for all variables, including the turbulent quantities, falls below the relative value of 10^{-5} (typically, 5000 to 15000 iterations are needed, depending on the specific tube and on the heat flux level), reducing by 5 orders of magnitude form the initial value.

As the main output of the simulations, after the check for grid convergence, the surface average temperatures, computed on the cells corresponding to the location of the sensible part of the thermocouples (see below) have been compared to the experimental values.

4.2 Computed results for the IS tube

The simulations on the Inconel® smooth tube have been performed taking advantage of the symmetry of the problem with respect to a plane passing through the tube axis and the focus of the parabolic concentrator. The mesh giving grid-independent results for both the speed and temperature field is shown in Figure 10: it consists of polyhedral cells with 10 prisms layers (the flow regime is turbulent) of a total thickness of ~ 0.6 mm with y+ at the wall ~ 1, as the Prandtl number is ~ 1 in all tested conditions. The total number of cells is ~ $3 \cdot 10^5$. The polyhedral mesher has been preferred to a tetrahedral because it allows obtaining better results in terms of accuracy and convergence of the solution, for a given number of cells, decreasing the mesh size needed to achieve grid-independent results.

The results of the grid convergence study, carried out to ensure that numerical results were independent on the chosen spatial discretization, are reported in Figure 11a and Figure 11b for the TK2 temperature and the mean outlet velocity, respectively. Figure 11 shows that an increase in the number of cells to 10^6 wouldn't lead to appreciably difference in the selected quantities, proving the grid independence of the computed results. Note that the quality of the mesh (skewness, smoothness) was carefully checked for all the different meshes used in the convergence analysis (see [45]).
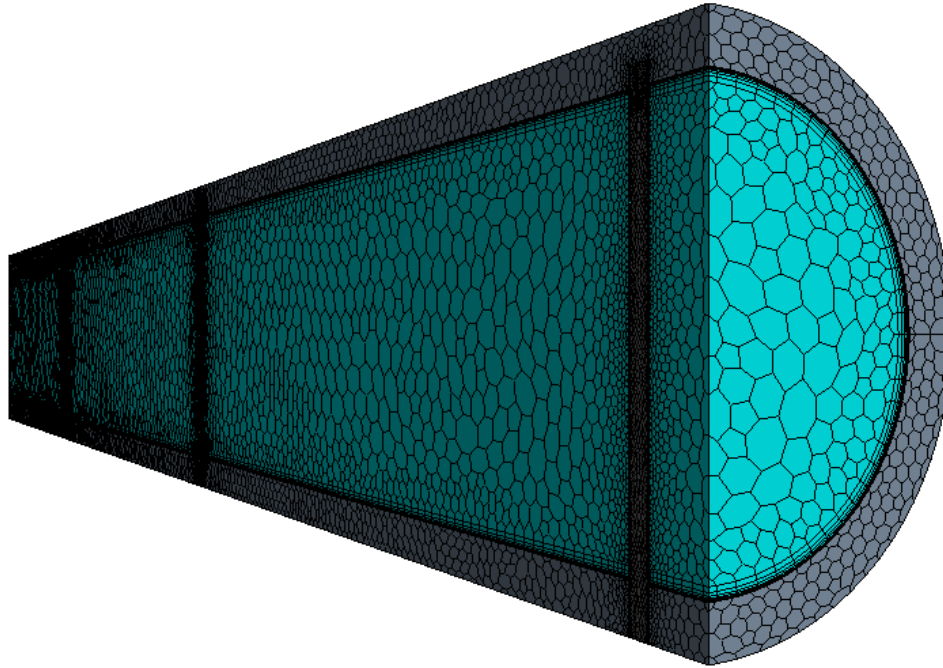
Figure 10 - Mesh used for the simulations on the IS tube. The solid domain is in grey, while the fluid domain is in light blue. Also, the three thermocouples (vertical bars) are shown.
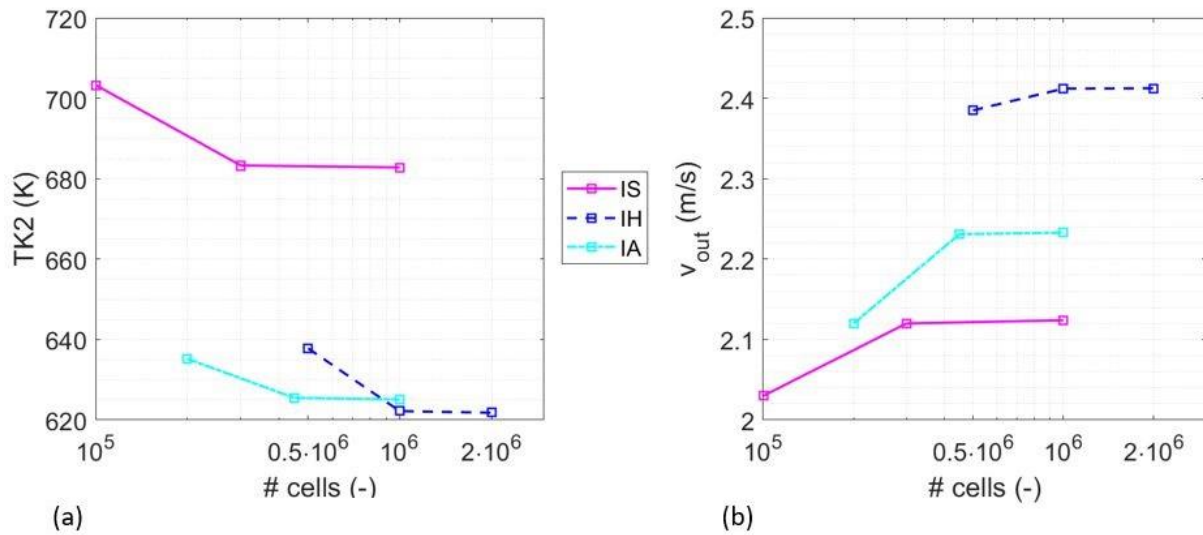

Figure 11 – Grid convergence results shown for (a) the TK2 temperature and (b) the mean outlet velocity, respectively, for three grids with increasing number of cells. The results for IS (solid lines), IA (dashed lines) and IH (dash-dotted lines) are reported.

Calibration

The calibration of the surface optical parameters has been performed decoupling ε and α as follows: first, the test IS1 (in "as-received conditions") has been used to calibrate a uniform absorption factor on the irradiated tube side, taking advantage of the fact that no oxidation was occurred yet, using Eq.16 at the same time to compute *locally* the value of ε. The value of α was calibrated to 0.33 on the entire surface

to give a good agreement with the experimental temperatures measured by the thermocouples TK1-TK2-TK3. The resulting emissivity map, naturally following the Gaussian shape of the heat load, which drives the temperature distribution on the exposed surface, has a peak value of 0.28, see Figure 12. Note that, as the power focal diameter (26.2 cm, Figure 3b) is larger than the tube length (210 mm), the emissivity is expected to be larger than the value extrapolated at ambient temperature (see Figure 9) all along the pipe, as actually visible in Figure 12.

Emissivity					
0.250	0.256	0.262	0.268	0.274	0.280
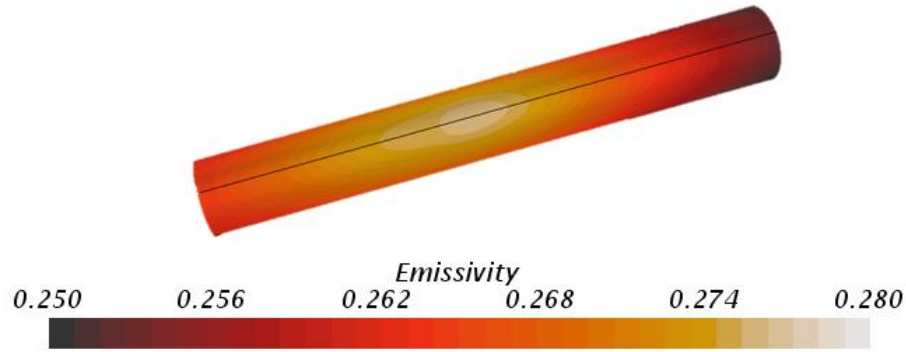
Figure 12 – Map of the emissivity value ε, resulting from the calibration based on the IS1 test results.

For the other two calibration tests, and namely IS2 and IS4, the same Gaussian shape of the thermal driver has been assumed also for α. This is a consequence of the fact that, after the first irradiation, the tube begins oxidizing on the irradiated surface and the oxidation effect is stronger where the local incident heat flux is higher. Since, however, no correlations for ε and α has been found in the literature for the specific material and for the different oxidation levels, the offset between their peak values (α_{peak} and ε_{peak}, respectively) has been computed in the calibration phase simulating the experimental test IS1 (see Eq.17), and then kept frozen to that value. The peak value is then used to set the define the Gaussian distribution for ε and α on the irradiated side, as from (Eq.1), where the peak incident heat flux φ_{peak} is replaced by ε_{peak} and α_{peak}, respectively.

$$\alpha_{peak} - \varepsilon_{peak} = 0.05 \qquad\qquad (Eq.17)$$

In practice, for the two cases IS2 and IS4, the value of α_{peak} was changed first, to match the measured temperatures, see Figure 13. Then, based on the value of α_{peak}, the value for ε_{peak} was computed from Eq.17. Note that, as the power focal diameter is larger than the tube length, also the value of the "baseline" absorptivity α_{base} (corresponding to the asymptotic value of the Gaussian distribution) was then increased to allow a good match between computed and experimental values for the cases IS2 and IS4, as reported in Figure 13. The α_{base} value in the "as-received" conditions was set to 0.33, i.e. the uniform absorptivity value used in the IS1 test, and then it was slightly increased to match the experimental data, following the expectation to have for α_{base} a smaller variation (lower slope of the trend line) than α_{peak}, since the oxidation out of the peak is weaker.
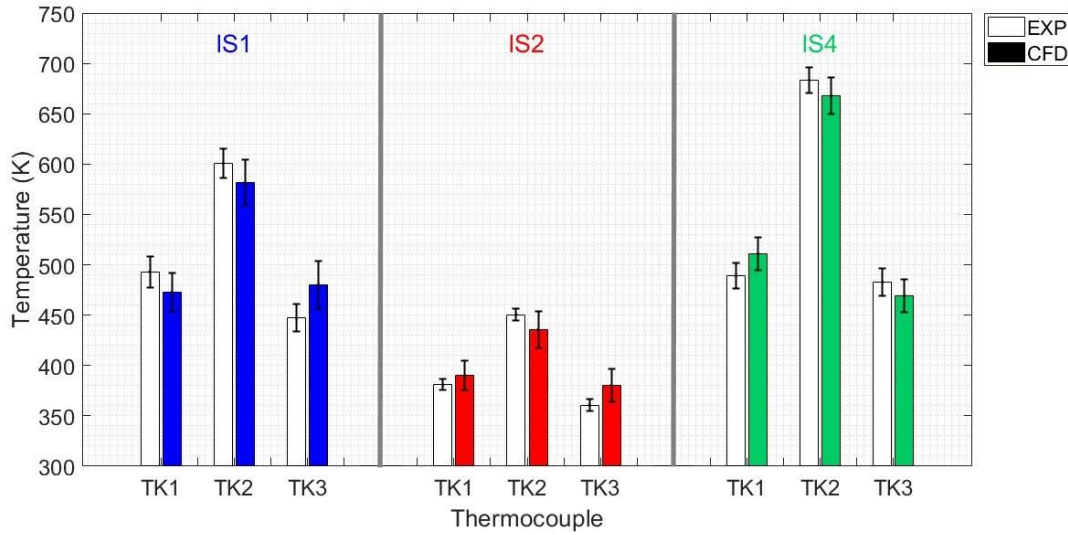
Figure 13 - Calibration simulations on the IS1 case (blue), the IS2 case (red) and the IS4 case (green), at ~180 kW/m², ~55 kW/m² and again ~180 kW/m², respectively. White bars for experimental data and solid bars for CFD results.

While in Figure 13 the experimental error-bar is reported, based on the thermocouples reading, the numerical error is estimated considering different contributions:

- The discretization error, which could be assessed through the Richardson extrapolation or the Grid Convergence Index (GCI). The latter has been evaluated here by means of the approach proposed by Celik [44], resulting in a GCI ~ 1.5%.
- The uncertainty coming from the errors on the radiometer and the flow meter reading: different simulations have been performed to cover all the possible combinations of power and flow rate. More in detail, if the two errors are independent, the maximum of the error bar is obtained through the maximum peak heat flux and the minimum air flow rate, and the opposite is true for the minimum error-bar. Moreover, the CFD error bar should include also the maximum and the minimum temperatures of the sensible part of the thermocouples (in the model). It is then expected to have larger error-bars for the CFD results when the heat flux level increases (because of the ±3% of the radiometer, which weighs more).

The values of α_{peak}, α_{base} and ε_{peak} computed from the calibration exercise as a function of the cumulated irradiated energy E_{cum} is reported in Figure 14: the computed trend lines (Eqs.18-19-20) allowed getting a suitable value for any of the test conditions for all the different Inconel® tubes. Based on that calibration, it was then possible to evaluate the emissivity and the absorptivity of all the experimental tests presented in Figure 6 and Figure 7. If some assumptions were needed to go through this calibration exercise, the good results obtained then for the three different CFD models at any cumulative irradiated energy will demonstrate the robustness of the methodology.

$$\alpha_{peak} = 0.33 + 4.0 \times 10^{-4} \cdot E_{cum} \qquad (Eq.\,18)$$

$$\alpha_{base} = 0.33 + 1.0 \times 10^{-4} \cdot E_{cum} \qquad (Eq.\,19)$$

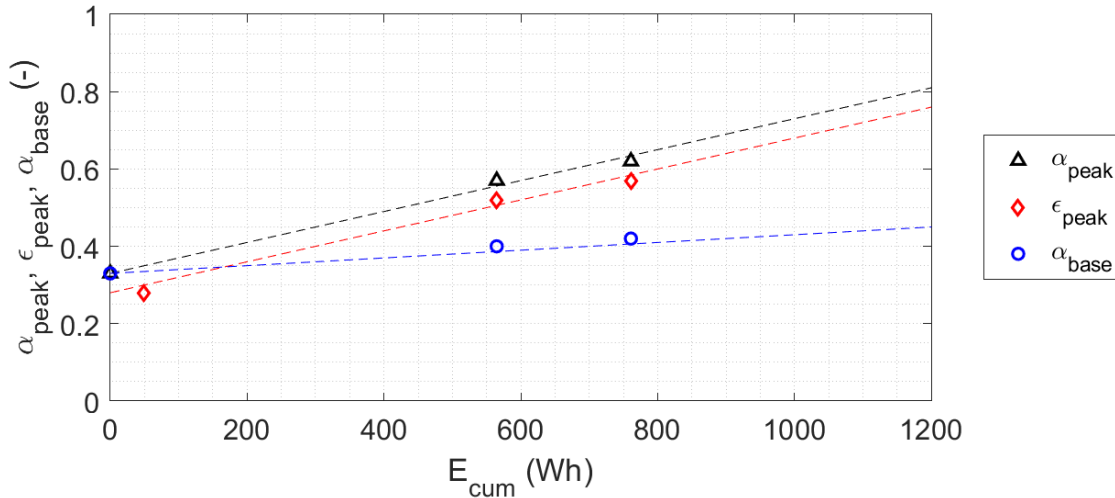$$\varepsilon_{peak} = 0.28 + 4.0 \times 10^{-4} \cdot E_{cum} \qquad (Eq.\,20)$$

Figure 14 – Variation of the peak and base absorptivity and peak emissivity with the cumulative irradiated energy: values from the calibration on the IS sample (symbols) and trendlines (dashed lines).

Validation

The validation of the recipe adopted for ε_{peak}, α_{peak} and α_{base} in the present analysis has been performed on the remaining two tests of the IS tube, namely IS3 and IS5. The comparison between computed and experimental results has been reported in Figure 15, showing that the simulations very well reproduce the measured temperature values, within the error-bars. Although the peak temperature is measured by means of TK2, the other two thermocouples are precious for the validation of the model. In addition, TK3 provides info on the quality of the simulation downstream of the peak load, where the temperature is *computed* by transport equations, not directly driven by the heating as in TK2.
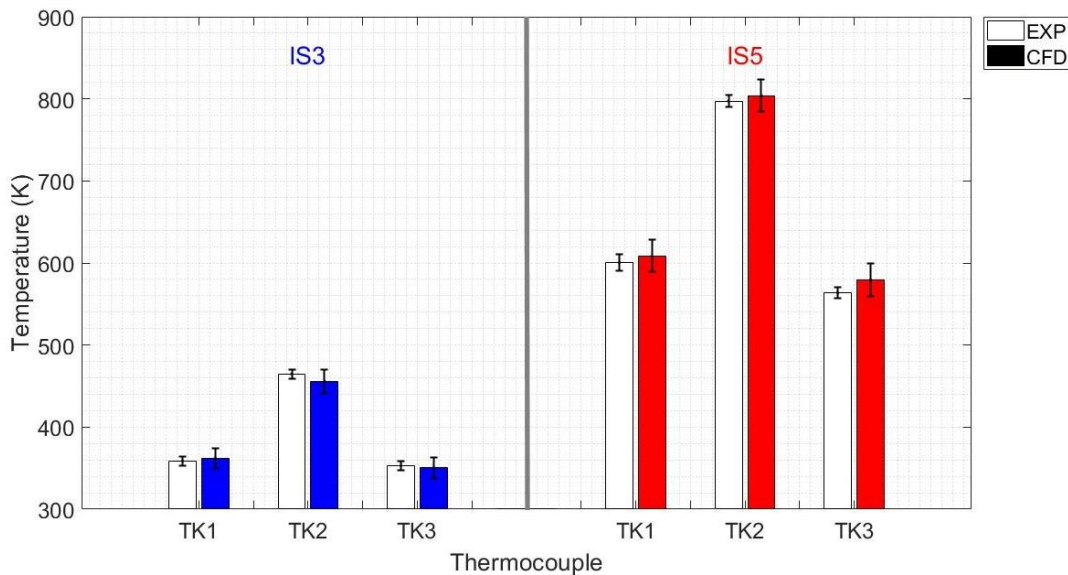
Figure 15 – Validation on the IS3 case (blue) and the IS5 case (red), at ~55 kW/m² and ~280 kW/m², respectively. White bars for experimental data and solid bars for CFD results.

Since the sample was manufactured through additive manufacturing, different roughness levels were investigated parametrically in the simulations, to check the effect of the surface roughness on the sample, and no major deviations from what is reported in Figure 15 were found for values of relative roughness varying from 0 (smooth tube) to 0.001, which are considered to be representative of the possible roughness range of the inner surface of the tube.

4.3 Computed results for the IA tube

The simulations on the Inconel® tube equipped with annular rings have been performed taking advantage of the symmetry of the problem with respect to a plane passing through the tube axis and the focus of the parabolic concentrator. The mesh giving grid-independent results for both the speed and the temperature field is shown in Figure 16: it consists of polyhedral cells with 10 prisms layers (the flow regime is turbulent) with y+ at the wall ~ 1 as the Prandtl number is ~ 1 in all tested conditions. The total number of cells is ~ $4.5 \cdot 10^5$ and the grid convergence is demonstrated in Figure 11. Note that the slight increase in the number of cells with respect to the IS sample is due to the need of resolving the ribs, which leads to a larger interface surface between the wall and the fluid.

The sequence of the tests performed on this sample has been reconstructed for the IA tube to evaluate E_{cum} for the tests IA1, IA4 and IA5, which are the ones considered in the CFD analysis. Since the tube material is the same of the sample IS, the trend lines of Eqs.18-19-20 can be used to derive suitable values for ε_{peak} , α_{peak} and α_{base}, used to define the Gaussian distribution of the optical properties in the simulation.
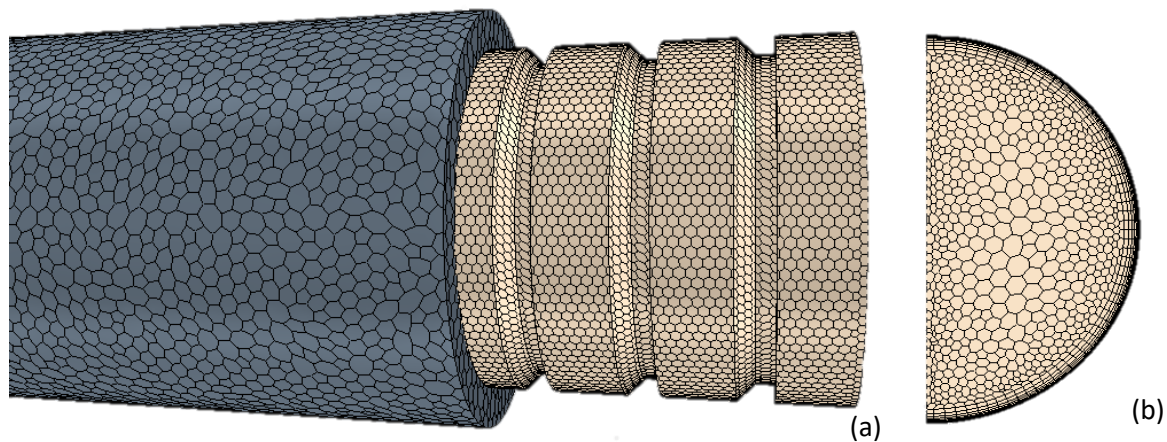

(a)

(b)

Figure 16 - Mesh developed for the simulation of the IA tube: (a) overview of a portion of the solid (grey) and fluid (pale pink) volume mesh; (b) representative cross section of the fluid domain.

The computed results for the IA1 test, i.e. the very first test in the "as-received" conditions, are compared to the experimental ones in Figure 17. The experimental temperatures from the thermocouples used during the experimental campaign are in very good agreement with the CFD results. This is also true for the other two levels of heat flux, as shown in Figure 17, confirming the robustness of the numerical model.
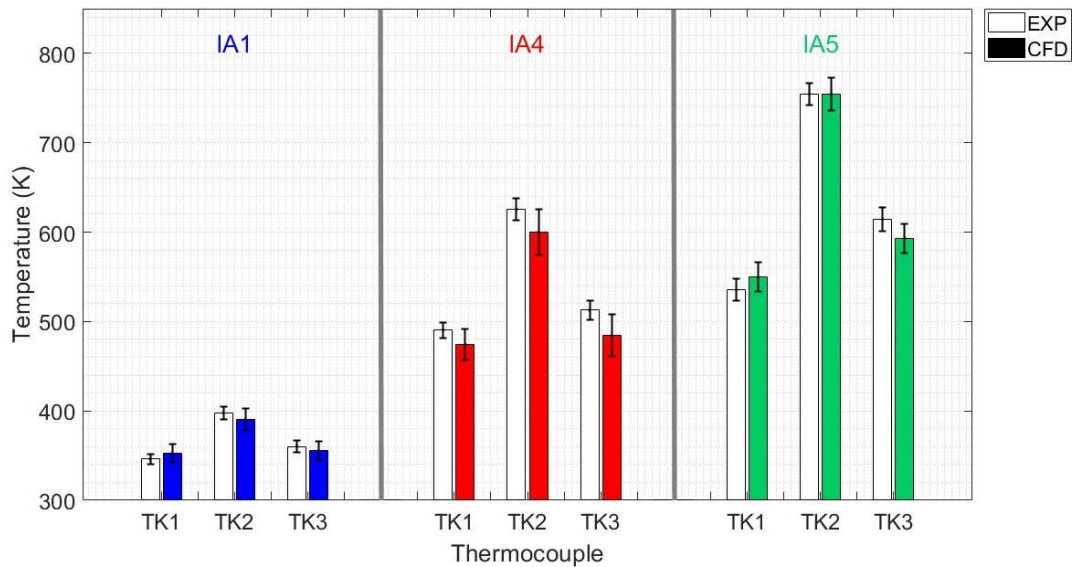
Figure 17 – Validation on the IA1 case (blue), the IA4 case (red) and the IA5 case (green), at ~55 kW/m², ~180 kW/m² and ~280 kW/m², respectively. White bars for experimental data and solid bars for CFD results.

4.4 Computed results for the IH tube

The simulations on the Inconel® tube equipped with the helical turbulence promoters were performed using the mesh (again giving grid-independent results for both the speed and temperature field) shown in Figure 18: it consists of polyhedral cells with 10 prisms layers with y+ at the wall ~ 1, with a resulting size of ~ 10^6 cells (see Figure 11 for grid convergence results). Note that the size of the mesh is roughly doubled with respect to the IA one, since the full IH tube has been simulated, and not just one half, because of the lack of symmetry.

(a)   (b)
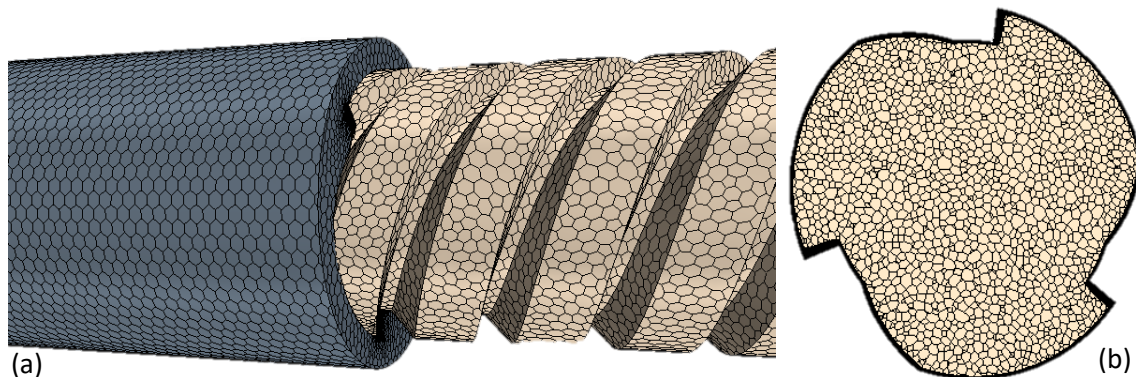
Figure 18 – Geometry developed for the simulation of the IH tube: (a) overview of a portion of the solid (grey) and fluid (pale pink) volume mesh; (b) representative cross section of the fluid domain.

For the optical properties to be used in the simulations for the IH tube, which turned out to be the most irradiated during the test campaign, the calibration performed for the IS tube (Eqs.18-19-20) was again used as in the case of the IA sample.

The computed results are reported in Figure 19, showing that the CFD temperatures and the experimental ones are in good agreement at all the different solar heat flux levels.
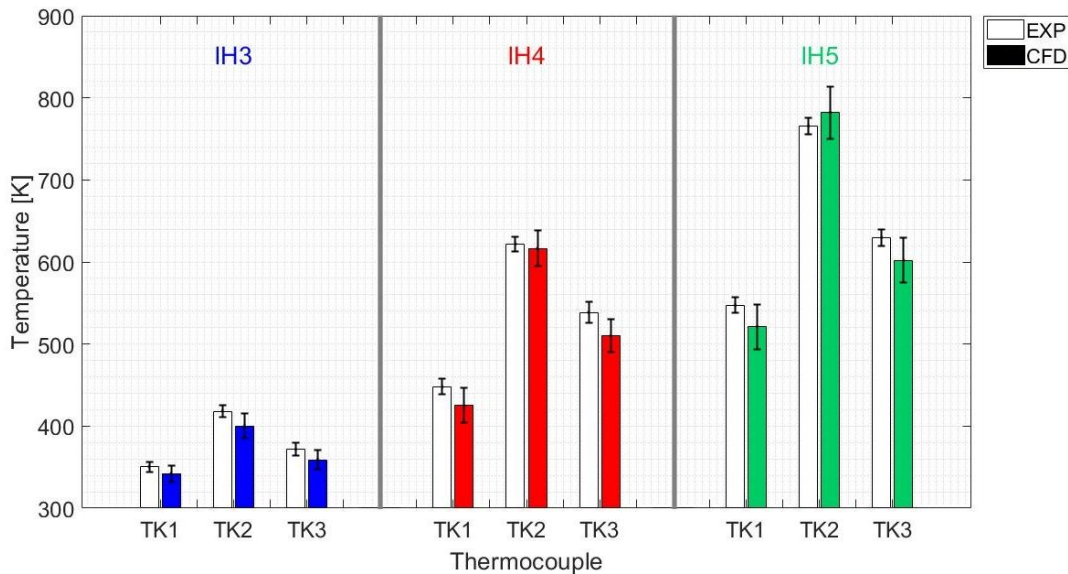

Figure 19 - Validation on the IH3 case (blue), the IH4 case (red) and the IH5 case (green), at ~55 kW/m², ~180 kW/m² and ~280 kW/m², respectively. White bars for experimental data and solid bars for CFD results.

5. Comparative performance of different turbulence promoters

Since the computational models have been validated through the experimental results, it is possible to compare fairly the three Inconel® tubes, equipped with the different turbulence promoters, in the same conditions (same irradiation and same oxidation level), a comparison which, as shown above, was not possible directly from the test results. The comparison has been then performed in the conditions listed below:

- Peak flux = 280 kW/m²: the highest level of heat flux has been chosen to show the different performance of the samples when the highest temperatures occur.
- Flow rate = 40 l/min (at 300 K), as in almost all the tests performed during the experimental campaign.
- α_{peak}= 0.8, as it is approximately the condition of the IH tube, which could represent the most interesting sample of the current work. Note that the value for α_{peak} refers to levels of E$_{cum}$ totally comparable to those reached by the IH sample.
- ε_{peak} = 0.75 and α_{base}= 0.45, according to Eqs.19-20.
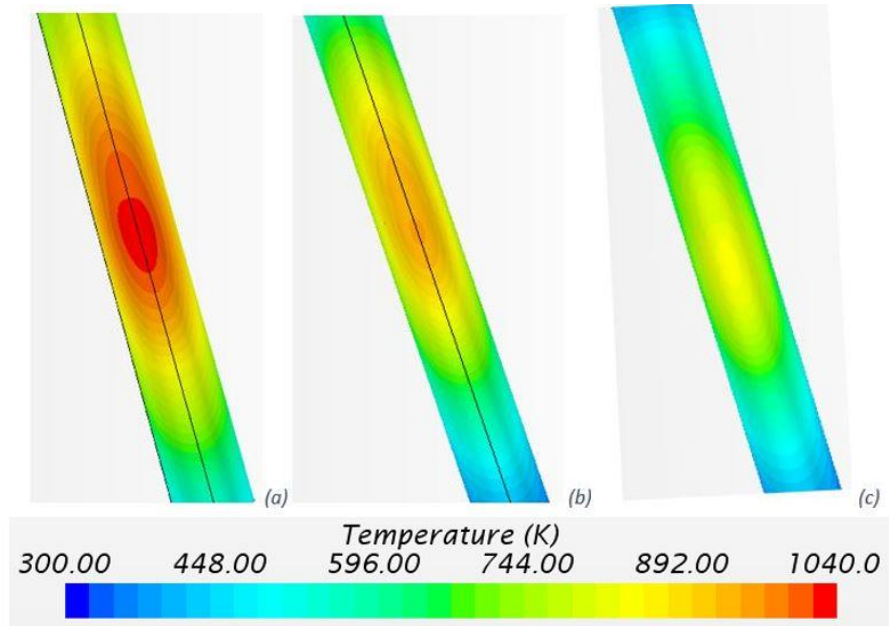
Figure 20 – Temperature maps computed on the irradiated surface of the IS (a), IA (b) and IH (c) tubes, respectively.

First, the maps of the computed temperature on the irradiated surface of the three different pipes are reported in Figure 20: as expected, the highest temperature is computed on the smooth tube, in view of the worse heat transfer to the coolant. The lowest temperature is computed for the IH, since it has the most effective turbulence promoter, while the IA tube presents an intermediate behaviour.

The temperature distribution computed on the surface of the IS tube leads to significant convective and radiative losses, if compared to the other two, as shown from the Sankey diagrams in Figure 21. In particular, as shown in Figure 21a, the radiative losses accounts for ~30% of the input power from the sun (net from the optical losses).
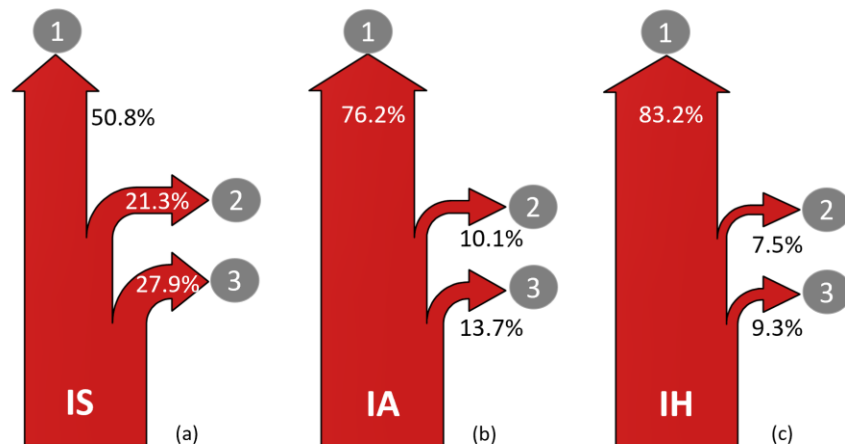

Figure 21 – Sankey diagram for the thermal power entering the pipes: the label "1" identifies the useful power to the fluid, the label "2" the convective losses and the label "3" the radiative losses for the IS (a), IA (b) and IH (c) tubes, respectively.

Being the aim of the turbulence promoters that of enhancing the heat transfer, the radiative and convective losses of the IA and IH tubes are lower, and the useful power to the fluid higher, than those computed for the IS tube, as clearly shown in Figure 21. Therefore, for IA and IH a larger bulk temperature of the air is expected at the outlet section. The simulations return the average value of 333 K, 358 K and 364 K at the outlet section of IS, IA and IH respectively.

Moreover, the flow pattern forced by the helices/rings allows having a more homogeneous temperature distribution. In Figure 22a, the radial profiles of the temperature at the outlet section of the three tubes are compared, showing that the gradient is much larger for the IS tube, with also a strong non-uniformity in the azimuthal direction, induced by the one-side heating. The air flow is not able to homogenise the tube temperature from the irradiated to the back side, and the temperature of the fluid along the axis still is ~ T_{amb}. On the contrary, when moving to the IA and, even more, to the IH tube, the mixing induced in the flow by the turbulence promotion drastically reduces the temperature gradient and azimuthal non-homogeneity.

Note that the reduced thermal gradient in the azimuthal direction for the IA and IH tubes will be beneficial for reduction of the thermal stresses in the receiver. However, the capability of the tubes equipped with turbulence promoters to transfer a larger power to the coolant, see Figure 21, results also in a larger temperature difference across the tube wall (~ 12.5 K and ~ 11.2 K for the IH and IA, respectively, to be compared to the ~ 7 K for the IS tube, at the location of the peak flux). In other words, the lower temperature peak in the IA and IH is reached at the expense of a larger temperature difference in the radial direction inside the tube wall.
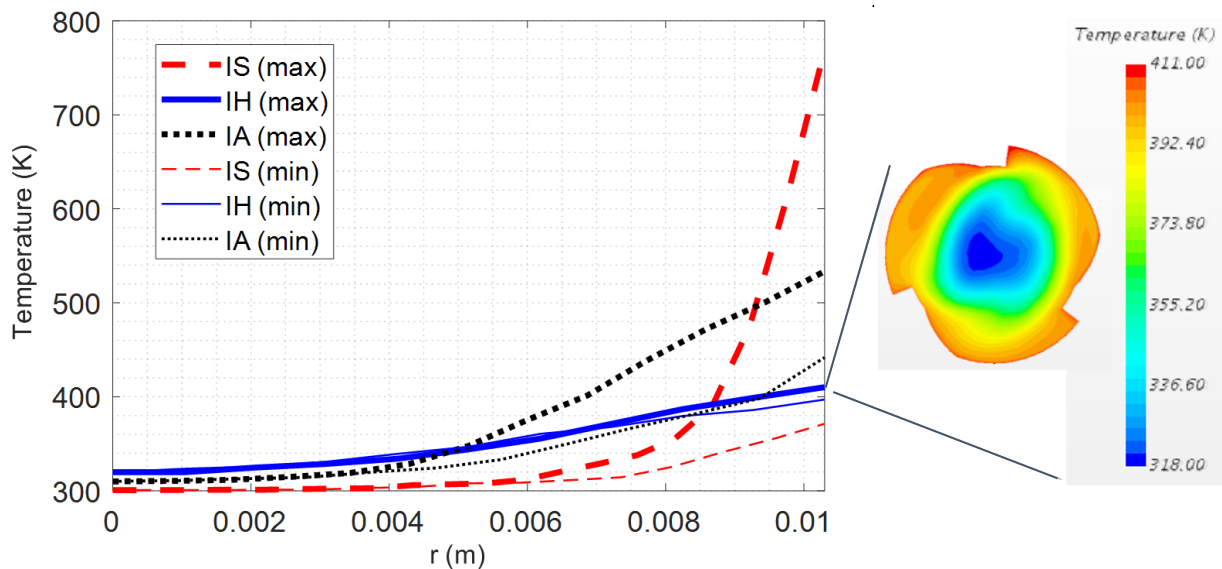

Figure 22 – Temperature radial profile computed at the tube outlet, along the line with maximum (thick lines) and minimum (thin lines) temperature difference between the tube centre and the wall, for the IS (dashed lines), IS (solid lines) and IA (dotted lines) tubes, respectively. In the inset: temperature map computed on the outlet section for the IH tube.

If looking more in depth to the flow field of the IA case, see Figure 23a, the streamlines of the core flow indicate that the coolant there is able to proceed along a straight path (perturbed just by the presence of the thermocouples). Close to the wall, instead, the detachment of the shear layer is visible, which is peculiar of the flow structure in tubes with periodic ribs (inset in Figure 23a), as already documented in

[32] for the width-to-pitch ratio of the IA tube. That ratio was indeed selected in the design phase to avoid the reattachment of the shear layer, that would have reduced the gain in the heat transfer enhancement.

For the IH case, the beneficial effect of the flow swirling induced by the turbulence promoters is evident from the plot of the streamlines along the tube, reported in Figure 23. The fluid particles attached to the internal wall follow the helices trajectory along the circumference, promoting the mixing of the fluid and contributing to the heat removal from the irradiated side to the back side of the tube wall. The resulting temperature map on the cross section at the outlet section, reported in the inset of Figure 22, shows a very limited memory of the one-side heating.
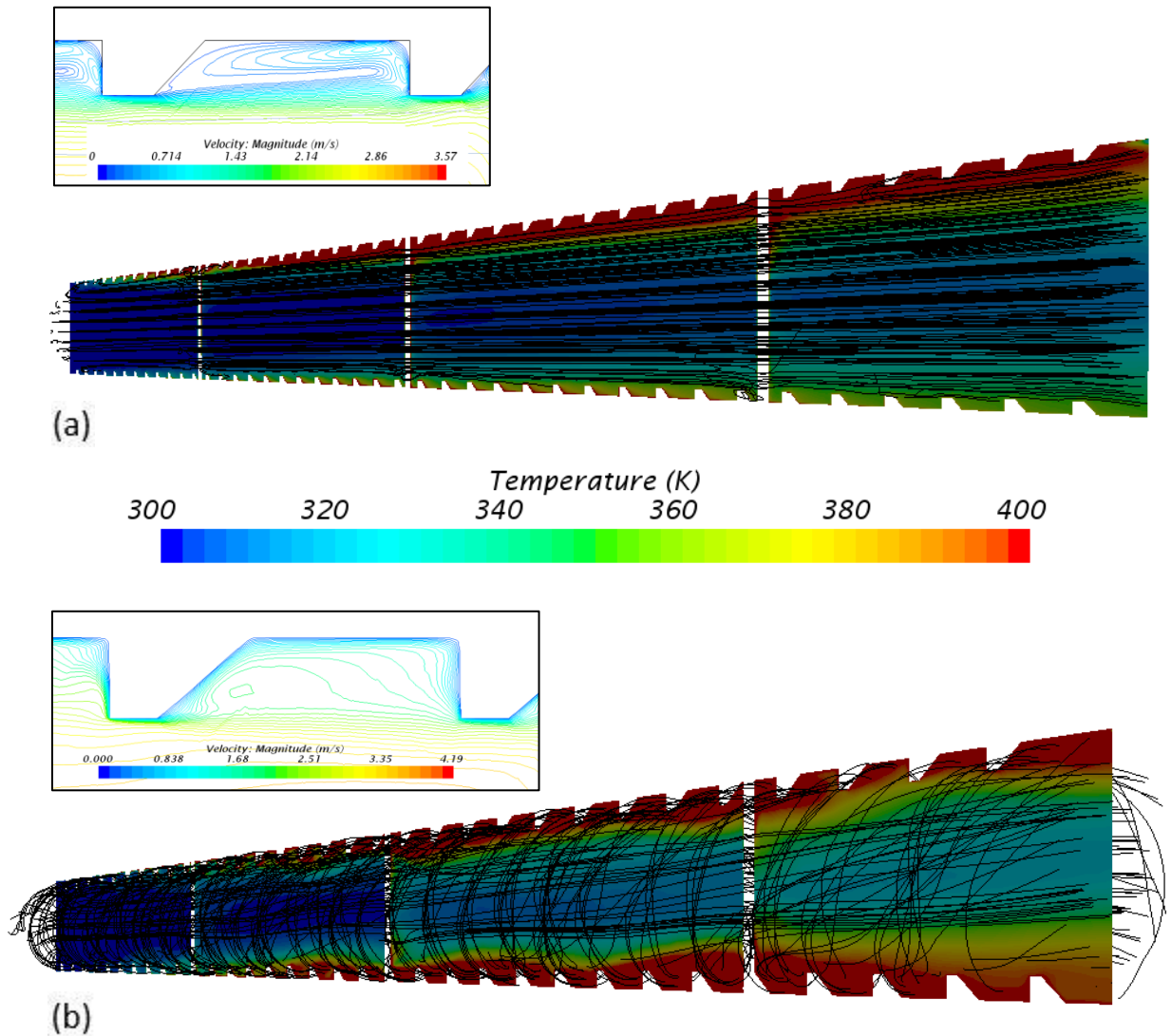

Figure 23 – Computed streamlines of the coolant in the IA sample (a) and IH sample (b), respectively, plotted on the background of the fluid temperature computed on the symmetry plane of the IA tube (and on the corresponding surface for the IH sample), with the maximum value clipped to 400 K. In the inset, on the same plane, an insight of the flow field between two adjacent ribs under the focus point are reported for the IA and IH, respectively.

From the computed results, a local heat transfer coefficient HTC, and then local and average Nu number could be derived from the definition reported in Eqs.21-22-23, respectively:

$$HTC(\zeta) = \frac{\overline{Q_{wall}(\zeta)}}{(\overline{T_{wall}(\zeta)} - T_{bulk}(\zeta))} \qquad (Eq.\,21)$$

$$Nu(\zeta) = \frac{HTC(\zeta) \times D_i}{k_{air}(\zeta)} \qquad (Eq.\,22)$$

$$\overline{Nu} = \int_0^L Nu(\zeta)\,d\zeta = D \int_0^L \frac{\overline{Q_{wall}(\zeta)}}{k_{air}(\zeta) \cdot (\overline{T_{wall}(\zeta)} - T_{bulk}(\zeta))}\,d\zeta \qquad (Eq.\,23)$$

where $\overline{Q_{wall}(\zeta)}$ is the azimuthally averaged wall heat flux transferred from the wall to the fluid at the local coordinate ζ on the wall-air interface surface, in W/m². The value is calculated automatically by the software by integration across the solid-fluid interface (neglecting the thermocouples), at a given ζ. $\overline{T_{wall}(\zeta)}$ is the azimuthally averaged interface (wall) temperature at the local coordinate ζ, $T_{bulk}(\zeta)$ is the bulk air temperature at the coordinate ζ (computed as a mass-flow average) and k_{air} is the air conductivity, evaluated at the local average wall temperature of the coolant.

A first comparison on the distribution local Nu(ζ) profile along the rib-roughened inner profile of the IA and IH tubes, compared to that of the smooth tube, is shown in Figure 24. The local enhancement of the heat transfer is clear, as also the larger effect (larger peak) in the IH sample. The distribution of Nu(ζ) for the IA tube is in agreement with published literature, and the minimum is computed at the end of the backward-facing edge (F-0 in the inset in Figure 24), as coherent with the flow field there, shown in the inset of Figure 23a. In the IH sample, the presence of a strong longitudinal component of the flow field (see the inset of Figure 23b) causes the displacement of the location of the minimum of Nu(ζ) slightly downstream of the end of the backward-facing edge (C-0 in the inset in Figure 24).
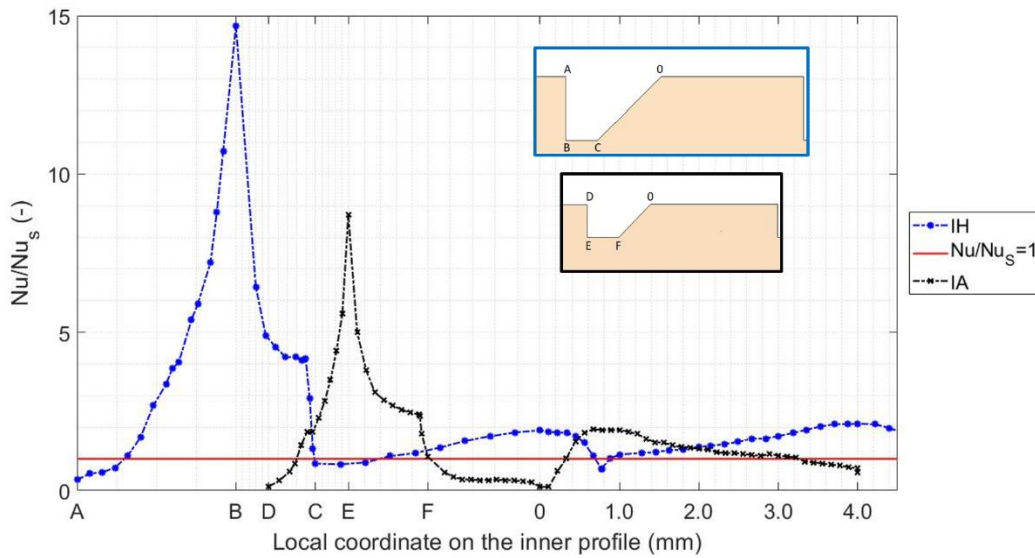

Figure 24 – Distribution of computed local Nusselt number Nu(ζ), referred to the smooth tube value, on the rib closer to the location of the heat flux peak, for both the IH and IA samples. The flow direction is from left to right.

Looking now to the average values of the Nusselt number, for the IS tube the computed value of $\overline{Nu}$ from the CFD results, using Eq.22, turned out to be 52. That value can be compared to the values of ~ 68 and ~ 78, computed using the well-known Dittus-Boelter correlation and Sieder-Tate correlation, respectively [24]. The value resulting from CFD is much lower than those predicted by the classical correlations but the fact is not surprising since those correlations are applicable in case of fully developed turbulent flow, where also the thermal boundary layer should be fully developed, which is not the case at all here. The thermal boundary layer in fact develops just on one side, and we can imagine its thickness to be significantly influenced by the Gaussian shape of the heat load. The case of a uniform heat flux applied on the entire length of a long pipe, where we expect to have a fully developed thermal boundary layer, would be different, as reported for instance in [23]. In that case, indeed, the comparison to classical smooth-tube correlations for the Nu number was meaningful, since the developing length for the thermal boundary layer was much shorter than the pipe length.
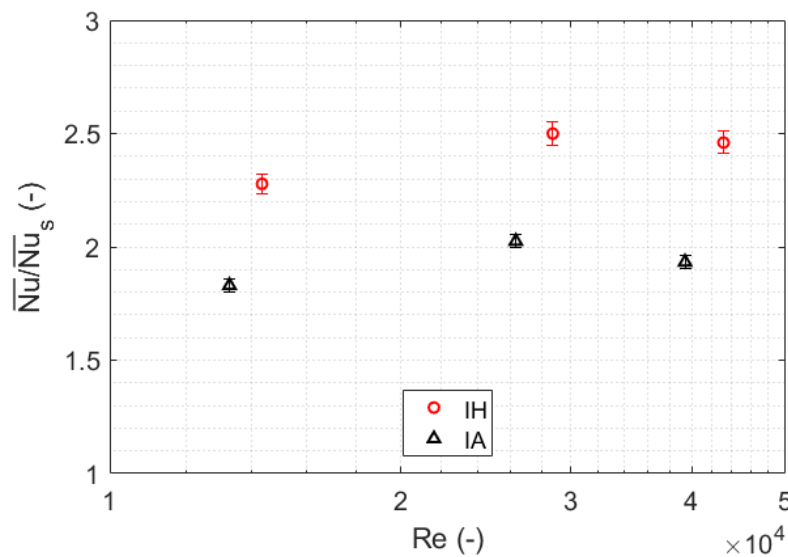

Figure 25 – Ratio between the computed average Nu for the tubes with turbulence promoters and that of the smooth tube, as a function of Re.

The increase of the heat transfer due to the turbulence promoters in the IA and IH samples, with respect to that of the IS, is shown in terms of the average Nusselt number $\overline{Nu}$ in Figure 25, and it is ~ 2 for the IA and ~ 2.4 for the IH, respectively. The two values are quite independent on the flow rate (Reynolds number Re), at least in the range 20 - 60 l/min (i.e., Re = 1.3×10^4 - 4.3×10^4)

To better compare the different tubes, which, beside the different thermal behavior also shows an associated different hydraulic behavior, the Thermal Enhancement Factor (TEF) [46] can be introduced. The TEF allows summarizing the results, weighting the two main phenomena [47] associated to the presence of turbulence promoters, and namely the increase of the heat transfer and the associated increase of pressure drop (which would determine a higher pumping cost).

The algebraic formulation of Eq.24, based on the modified Reynolds analogy [24], can be found in [48] and it is suitable to compare the thermal and hydraulic effects of flows inside smooth tubes and

"enhanced" tubes. A value of TEF >1 implies that the enhancement of the heat transfer brings more benefits than the penalty due to the increase of the pressure drop – note that the exponent of 1/3 in Eq.24 can be inferred from the same exponent of the Prandtl number in the modified Reynolds analogy.

$$TEF = \frac{\overline{Nu}\big/\overline{Nu_s}}{(f/f_s)^{1/3}} \qquad (Eq.\,24)$$

In Eq.24, $\overline{Nu}$ and $\overline{Nu_s}$ are the Nusselt numbers evaluated through CFD for the samples IA and IH ($\overline{Nu}$) and for the smooth tube IS ($\overline{Nu_s}$), respectively, while f and f_s are the friction factors, evaluated for the IA and IH samples (f) and for the IS sample (f_s), respectively, through the Darcy relation (Eq.25)..

$$f = \frac{2}{L/D_i} \frac{\Delta p}{\rho \bar{v}^2} \qquad (Eq.\,25)$$

In Eq.25, Δp is the computed pressure drop along the tubes, L is the tube Length, D_i is the inner (nominal) diameter of the tube, $\bar{v}$ is the average fluid speed on the inlet section, and ρ is the fluid density evaluated at the average bulk temperature along the tube.

The friction factor computed for the IS sample can be easily validated against the values expected based on well-known correlations such as the McAdams correlation (Eq.26) valid for turbulent flows in smooth pipes and for $10^4 < Re_{Di} < 3\cdot10^5$, or the Petukhov correlation (Eq.27) [48], valid for fully developed turbulent flows in pipes in the range $10^4 < Re_{Di} < 10^6$. The good agreement of the computed values of f_S is presented in Figure 26. As a rule of thumb, a 10% accuracy is expected for the empirical correlations [49].
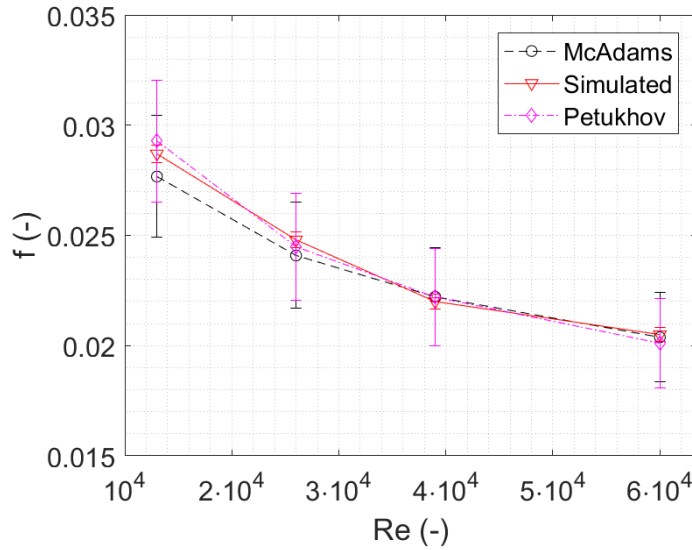

Figure 26 – Validation of the results on friction factor for the smooth sample: simulated vs empirical correlations.

$$f_s = 0.184 \cdot Re_{D_i}^{-0.2} \qquad (Eq.\,26)$$

$$f_s = \left[0.79 \cdot ln\left(Re_{D_i}\right) - 1.64\right]^{-2} \qquad (Eq.\,27)$$

If the value of the $\overline{Nu}/\overline{Nu}_s$ ratio, reported in Figure 27 for both IA and IH samples, already discussed above, demonstrate a significant increase of the heat transfer when considering the two samples with turbulence promoters, the gain of the IH sample over the IA sample is much more reduced than that indicated by the pure Nu number if the effect of the increase of the pressure drop (friction factor) is taken into account in the comparison. The values of the TEF for the IA and IH samples, as a function of different flow rates, are reported in Figure 27. At the lowest value of Re simulated here, the TEF is comparable for IA and IH (~ 1.2-1.4). The advantage of the IA configuration in terms of TEF tends to decrease as the Re number increases, while it remains stable around the value of 1.3-1.4 for the IH configuration.

Through parametric investigations, it was also possible to verify that the results in Figure 27 are not influenced by the level of oxidation and by the power level – a variation of α_{peak} from 0.4 to 0.8, or of the peak heat flux from 55 to 300 kW/m² leads to a TEF variation below 0.5%, much smaller of the uncertainty bar reported in Figure 27.
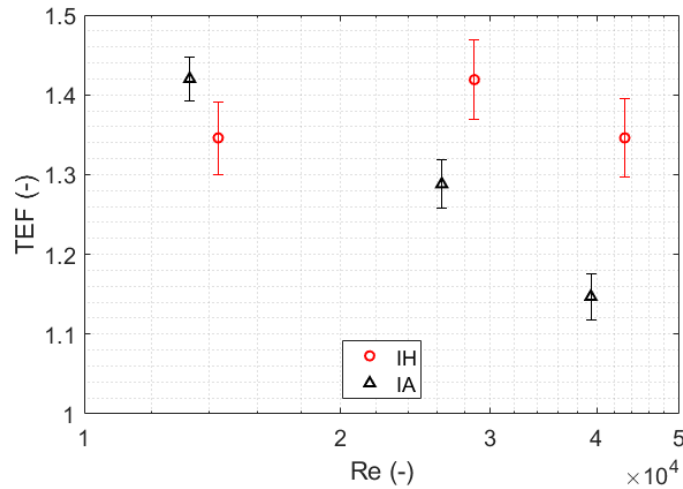

Figure 27 – TEF for the tubes equipped with turbulence promoters, as a function of Re.

As a final caveat, the TEF values computed above for IA and IH are based on average Nu values referring to a heat load that is axially very localized, with a thermal boundary layer that never reaches the full development. The possibility to extrapolate those values directly to full-scale tubular receivers, where the heat flux results from, e.g., an entire solar field in a central tower configuration, is to be checked.

6. Conclusions and perspective

This work presents an experimental campaign where three air-cooled absorber tube configurations have been tested at the Plataforma Solar de Almería SF60, with the aim of evaluating their thermal behavior under realistic conditions (one side heating) and providing data to calibrate and validate the Computational Fluid Dynamics models of the tested tubes. The use of repeated rib-roughness turbulence promoters has been experimentally demonstrated to reduce the wall temperature with respect to the

case of a smooth tube, although a quantitative comparison was not possible given the different oxidation state of the tubes during the tests at comparable heat load level.

Three different complex CFD models were developed for the smooth tube, for the helically ribbed configurations and for the tube equipped with rings, respectively. Few test results on the smooth tube were used to calibrate the increase of the surface emissivity and absorptivity due to the irradiation-induced oxidation: the trends found for ε and α in the calibration phase were proved to be robust, since they allowed computing a very good agreement on the temperatures measured and computed at thermocouples for all tubes and tests, out of the calibration ones.

The CFD models were then used to compare the three tubes under similar conditions of flow rate, heat load, oxidation. It turned out that the pure thermal performance, in terms of average Nusselt number, increases by a factor of ~2 and ~2.4 for the samples equipped with annular ribs and helical ribs, respectively, if compared to the smooth tube. However, among the two configurations of turbulence promoters, only the helical ribs can ensure a homogenization of the fluid temperature inside the tube, reducing dramatically the azimuthal thermal gradients. The Thermal Enhancement Factor, combining the heat transfer enhancement to the simultaneous increase of pressure drop, induced by the turbulence promoters, turned out to be ~ 1.4 for the tube with helical ribs, value which remains insensitive to flow rate, oxidation level and power level. That value, which has been assessed for a short tube with localized heating, needs to be confirmed for a full-scale application.

In perspective, the validated CFD models will become useful tools to optimize the geometry tubular receivers equipped with repeated rib-roughness turbulence promoters, to minimize the thermal gradients on the tube wall and to increase the lifetime of the component against thermal fatigue.

Acknowledgements

References

[1] Islam MT, Huda N, Abdullah AB, Saidur R. A comprehensive review of state-of-the-art concentrating solar power (CSP) technologies: current status and research trends. Renewable and Sustainable Energy Reviews 2018; 91:987–1018.
[2] Pavlovic TM, Radonjic IS, Milosavljevic DD, Pantic LS. A review of concentrating solar power plants in the world and their potential use in Serbia. Renewable and Sustainable Energy Reviews 2012; 16(6):3891–3902.
[3] First Green. Comparison of CSP technologies, 2012.
[4] Bhatia SC. Solar Thermal Energy. Advanced Renewable Energy Systems 2014; 94-143.
[5] Barlev D, Vidu R, Stroeve P. Innovation in concentrated solar power. Solar Energy Materials and Solar Cells 2011; 95(10):2703–2725.

[6] Li L, Coventry J, Bader R, Pye J, Lipinski W. Optics of solar central receiver systems: a review. Optics express 2016; 24(14): A985–A1007.

[7] Ho CK, Iverson BD. Review of high-temperature central receiver designs for concentrating solar power. Renewable and Sustainable Energy Reviews 2014; 29:835–846.

[8] Flores O, Marugán-Cruz C, Santana D, García-Villalba M. Thermal stresses analysis of a circular tube in a central receiver. Energy Procedia 2014; 49:354-362.

[9] Coventry J, Andraka C, Pye J, Blanco M, Fisher J. A review of sodium receiver technologies for central receiver solar power plants. Solar Energy 2015; volume 122, 749-762.

[10] Becker M, Böhmer M. Gast: The Gas Cooled Solar Tower Technology Program. Proceedings of the Final Presentation May 30-31, Lahnstein, Federal Republic of Germany Springer Verlag, 1989.

[11] DLR. Solhyco final public report - ses6-ct-2005-019830, 2011.

[12] Quero M, Korzynietz R, Ebert M, Jiménez AA, Del Río A, Brioso JA. Solugas–operation experience of the first solar hybrid gas turbine system at MW scale. Energy Procedia 2014; 49:1820–1830.

[13] Quero M, Korzynietz R, Ebert M, Jiménez AA, Del Río A, Brioso JA. Solugas–Operation experience of the first solar hybrid gas turbine system at MW scale SolarPACES 2013, Las Vegas, USA.

[14] Yang M, Yang X, Yang X, Ding J. Heat transfer enhancement and performance of the molten salt receiver of a solar power tower. Applied Energy 2010; 87(9):2808-2811.

[15] Uhlig R, Gobereit B, Rheinländer J. Advancing tube receiver performance by using corrugated tubes. Energy Procedia 2015; 69: 563-572

[16] Sethumadhavan R, Raja Rao M. Turbulent flow heat transfer and fluid friction in helical-wire-coil-inserted tubes. International Journal of Heat and Mass Transfer 1983; 26:1833-1845.

[17] Conroy T, Collins MN and Grimes R. A review of steady-state thermal and mechanical modelling on tubular solar receivers. Renewable and Sustainable Energy Reviews 2019; 119: 109591.

[18] Boerema N, Morrison G, Taylor R, Rosengarten G. High temperature solar thermal central-receiver billboard design. Solar Energy 2013; 97:356-368.

[19] Cagnoli M, de la Calle A, Pye J, Savoldi L, Zanino R. A CFD-supported dynamic system-level model of a sodium-cooled billboard-type receiver for central tower CSP applications. Solar Energy 2019; 177:576-594.

[20] Kim J, Kim JS, Stein W. Simplified heat loss model for central tower solar receiver. Solar Energy 2015; 116:314-322.

[21] Kim JS, Potter D, Gardner W, Too YCS, Padilla RV. Ideal heat transfer conditions for tubular solar receivers with different design constraints. In AIP conference proceedings 2017 (Vol. 1850, No. 1). AIP Publishing LLC.

[22] Pye J, Zheng M, Asselineau CA, Coventry J. An exergy analysis of tubular solar-thermal receivers with different working fluids. Proceedings of SolarPACES 2014.

[23] Zanino R, Bonifetto R, Cau F, Portone A, Savoldi Richard L. CFD analysis of the ITER first wall 06 panel. Part II: Thermal-hydraulics. Fusion Engineering and Design 2014; 89(4):431-441.

[24] Incropera F, DeWitt D. Introduction to heat transfer, 1985.

[25] Antoranz A, Gonzalo A, Flores O, Garcia-Villalba M. Numerical simulation of heat transfer in a pipe with non-homogeneous thermal boundary conditions. International journal of heat and fluid flow 2015; 55:45-51.

[26] Jianfeng L, Jing D, Jianping Y. Heat transfer performance of an external receiver pipe under unilateral concentrated solar radiation. Solar Energy 2010; 84(11):1879-1887.

[27] Rodríguez-Sánchez MR, Marugan-Cruz C, Acosta-Iborra A, Santana D. Comparison of simplified heat transfer models and CFD simulations for molten salt external receiver. Applied thermal engineering 2014; 73(1):993-1005.

[28] Marugán-Cruz C, Flores O, Santana D, García-Villalba M. Heat transfer and thermal stresses in a circular tube with a non-uniform heat flux. International Journal of Heat and Mass Transfer 2016; 96:256-266.

[29] D. Martínez-Plaza. General information plataforma solar de Almeria.

[30] PSA website, http://www.psa.es/es/index.php, last accessed on 02/02/20.

[31] http://sfera.sollab.eu/index.php, last accessed on 29/02/20.

[32] Webb RL, Eckert ERG, Goldstein R J. (1971). Heat transfer and friction in tubes with repeated-rib roughness. International Journal of Heat and Mass Transfer 1971; 14(4): 601-617.

[33] Roldán MI, Monterreal R. Heat flux and temperature prediction on a volumetric receiver installed in a solar furnace. Applied energy 2014; 120:65–74.

[34] Ballestrın J, Ulmer S, Morales A, Barnes A, Langley LW, Rodrıguez M. Systematic error in the measurement of very high solar irradiance. Solar energy materials and solar cells 2003, 80(3):375–381.

[35] Bronkhorst high tech. Datasheet f-203av. mass flow controller for gases.

[36] Greene GA. Dependence of total hemispherical emissivity of Inconel-718 on surface oxidation and temperature. Technical report, Brookhaven National Lab., Upton, NY (US), 1999.

[37] Malalasekera W, Versteeg HK. An introduction to computational fluid dynamics. The finite volume method, Harlow: Prentice Hall, 2007.

[38] Menter, F.R. Two-Equation Eddy-Viscosity Turbulence Models for Engineering Applications. AIAA J. 1994, 32, 1598–1605.

[39] Mohammadi O, Pironneau B. Analysis of the k-eps turbulence model. Wiley, 1994.

[40] Stoddard MC. Convective loss measurements at the 10 MW/sub e/Solar Thermal Central Receiver Pilot Plant (No. SAND-85-8250, 1983). Sandia National Labs, Livermore, CA (USA).

[41] Rodríguez-Sanchez MR, Soria-Verdugo A, Almendros-Ibanez JA, Acosta-Iborra A, Santana D. Thermal design guidelines of solar power towers. Applied Thermal Engineering 2014; 63(1):428–38.

[42] Gartner D, Johannsen K, Ramm H. Turbulent heat transfer in a circular tube with circumferentially varying thermal boundary conditions. International Journal of Heat and Mass Transfer 1974; 17(9):1003–18.

[43] Abbasi-Shavazi E, Hughes GO, Pye JD. Investigation of heat loss from a solar cavity receiver. Energy Procedia 2015; 69:269–278.

[44] Celik IB, Ghia U, Roache PJ, C. J. Freitas. Procedure for estimation and reporting of uncertainty due to discretization in CFD applications. Journal of fluids Engineering-Transactions of the ASME 2008; 130(7).

[45] Siemens PLM Software Inc., Star-CCM+ User's Guide v 14.02; Plano, TX, USA, 2019.

[46] Wongcharee K, Changcharoen W, Eiamsa-Ard S (2011). Numerical investigation of flow friction and heat transfer in a channel with various shaped ribs mounted on two opposite ribbed walls. International Journal of Chemical Reactor Engineering 2011; 9(1).

[47] Moon MA, Park MJ, Kim KY. Evaluation of heat transfer performances of various rib shapes. International Journal of Heat and Mass Transfer 2014; 71:275-284.

[48] Webb RL, Kim NH. Principles of Enhanced Heat Transfer, Taylor & Francis, New York, NY, USA, 2nd edition, 2005.

[49] Munson BR, Young DF, Okiishi TH. Fundamentals of fluid mechanics, 1998.